minerals

MDPI

Article

Tectonometamorphic Evolution of the Migmatitic Paragneisses of the Filali Unit (Internal Rif, Morocco)

Abdelkhaleq Afiri [1,*], Abderrahim Essaifi [2], Ali Charroud [3], Mourad Aqnouy [4], Kamal Abdelrahman [5], Amar Alali [4] and Mohamed Abioui [6,7,*]

[1] Applied Geology Research Laboratory, Department of Geosciences, Faculty of Sciences and Techniques, Moulay Ismail University of Meknes, Errachidia 52000, Morocco
[2] Lithosphere Dynamics and Resource Genesis Laboratory "DLGR" (Unit Associated with CNRST, URAC 43), Department of Geology, Faculty of Sciences-Semlalia, Cadi Ayyad University, Marrakech 40000, Morocco
[3] Department of Geosciences, Faculty of Sciences and Techniques, Moulay Ismail University of Meknes, Errachidia 52000, Morocco
[4] Applied Geology Research Laboratory, Applied Geology and Remote Sensing Research Team, Department of Geosciences, Faculty of Sciences and Techniques, Moulay Ismail University of Meknes, Errachidia 52000, Morocco
[5] Department of Geology & Geophysics, College of Science, King Saud University, Riyadh 11451, Saudi Arabia
[6] Geosciences, Environment and Geomatics Laboratory (GEG), Department of Earth Sciences, Faculty of Sciences, Ibnou Zohr University, Agadir 80000, Morocco
[7] MARE—Marine and Environmental Sciences Centre-Sedimentary Geology Group, Department of Earth Sciences, Faculty of Sciences and Technology, University of Coimbra, 3030790 Coimbra, Portugal
* Correspondence: afiriabdelkhaleq@yahoo.fr (A.A.); m.abioui@uiz.ac.ma (M.A.)

Abstract: A lithosphere-scale extensional shear zone juxtaposes an underlying sub-continental peridotite body and overlying migmatitic paragneisses of the Filali unit in the Beni Bousera massif (Internal Rif, Morocco). Three stages are recognized in the metamorphic evolution of the aluminous paragneiss, marked by the chemical zoning of garnet porphyroblasts and the evolution of associated mineral assemblages characterized by the presence of kyanite and rutile (M1), sillimanite, k-feldspar and melt (M2), and cordierite (M3). Phase-equilibrium modeling (pseudosections) and multi-equilibrium thermobarometry point to P-T conditions of 7 kbar 750 °C and 3.5 kbar 685 °C for the M2 and M3 stages, respectively. M1 conditions of 9.3 kbar 660 °C were inferred using modeling after the reintegration of melt lost during M2 into the bulk composition. Published geochronological data suggest a Variscan age (250–340 Ma) for the M1 event, whereas M2 and M3 are Oligo-Miocene and related to the Alpine orogeny. The recorded sub-isothermal decompression is related to significant crustal attenuation in the Oligo-Miocene and is responsible for the juxtaposition of the hot asthenospheric mantle and the crustal units, causing the melting of the paragneiss. The exhumation of the gneisses by crustal extension is associated with the westward retreat of an Alpine subduction (slab rollback).

Keywords: migmatitic paragneisses; sub-isothermal decompression; pseudosections; partial melting; melt reintegration; Rif belt

Citation: Afiri, A.; Essaifi, A.; Charroud, A.; Aqnouy, M.; Abdelrahman, K.; Alali, A.; Abioui, M. Tectonometamorphic Evolution of the Migmatitic Paragneisses of the Filali Unit (Internal Rif, Morocco). *Minerals* **2023**, *13*, 484. https://doi.org/10.3390/min13040484

Academic Editor: Rubén Díez-Fernández

Received: 26 February 2023
Revised: 25 March 2023
Accepted: 27 March 2023
Published: 30 March 2023

1. Introduction

The Betic-Rif belt is located at the western termination of the peri-Mediterranean Alpine orogenic system (Figure 1a). This orogenic belt is thought to be the result of a collision between the African and Eurasian plates and Alboran blocks during the Alpine orogeny [1–7]. The geodynamic evolution of this belt has been a matter of strong debate because of its polyphase tectonometamorphic history involving the Variscan and Alpine orogenies [8,9]. The metamorphic rocks show the superposition of several mineral assemblages showing a contrasted geothermal gradient and, therefore, different tectonic contexts [10,11]. Variscan and Alpine ages have been recorded in the metamorphic rocks [9,12–18]. The

Betic-Rif chain is also characterized by a series of ultramafic bodies of outcrops of varying extents in a crustal metamorphic envelope, the largest of which is the Ronda massif in southern Spain and Beni Bousera in northern Morocco [19,20]. The uncertainties regarding the structural and thermal evolution of the high-grade metamorphic units in the Alboran domain have led to contrasting tectonic models for the emplacement of the peridotites. The polymetamorphic evolution (Alpine or Variscan), as well as the ages and processes of the juxtaposition of high-temperature (HT) metamorphic rocks with the peridotite bodies, remain particularly debated in this region (see the review in [6,9,13,21,22]).

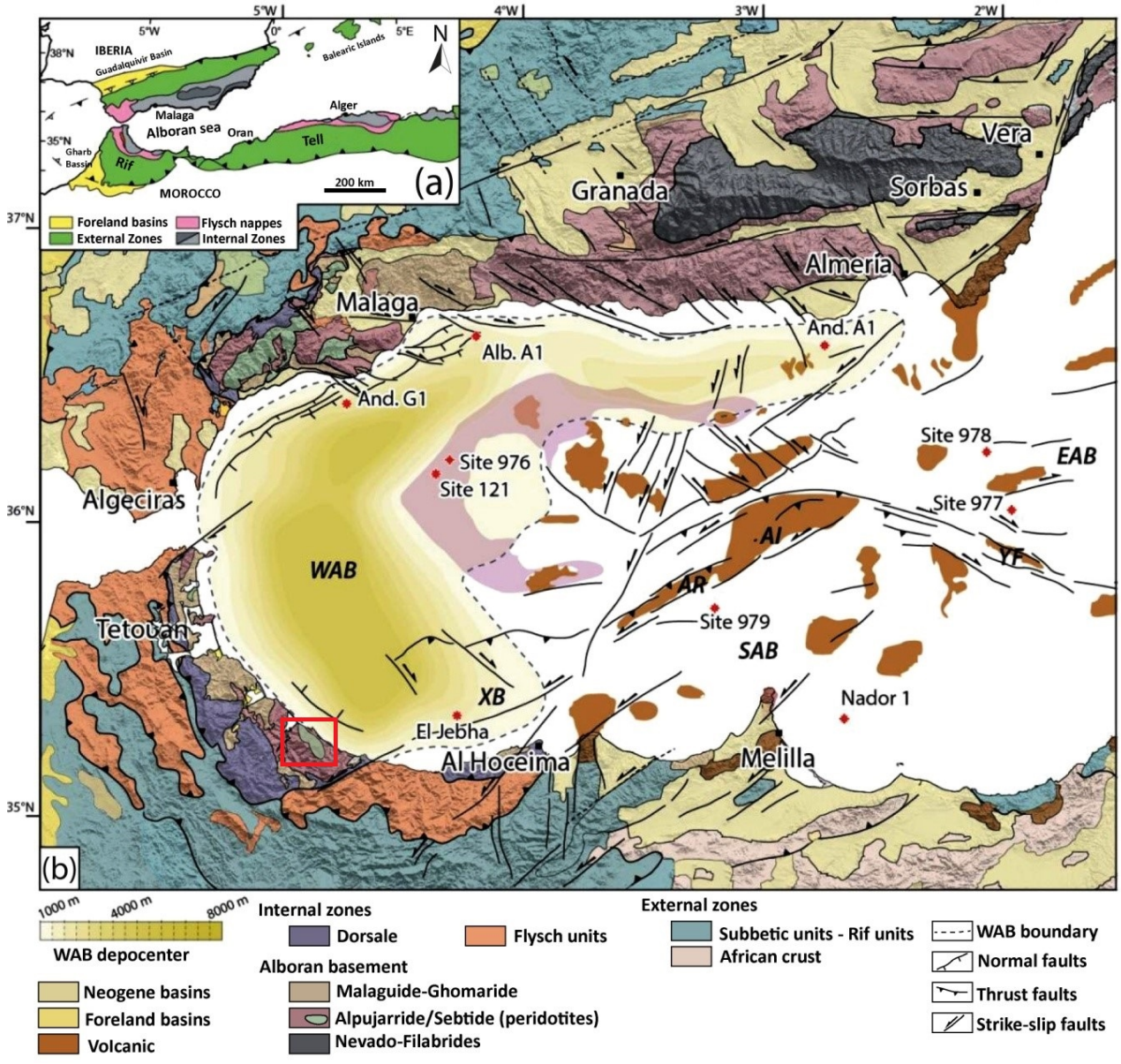

Figure 1. Geologic map of the Alboran domain in the Betic-Rif arc with the major tectonic features, modified after Do Couto et al. [1]. (**a**) Location of the studied mountain belt within the Gibraltar arc. (**b**) Detailed geologic and tectonic map of the chain, centered on the Rif and zooming on the Internal zones, with the location of the investigated area (open red box). ODP sites 976 to 979, DSDP site 121, and all industrial wells are also located offshore (And G1 = Andalucía-G1; Alb A1 = Alborán-A1; And A1 = Andalucía-A1). AR = Alboran ridge; AI = Alboran Island; EAB = Eastern Alboran Basin; SAB = South Alboran Basin; WAB = western Alboran Basin; XB = Xauen bank; YF = Yusuf fault.

Recent progress in phase equilibria modeling combined with the examination of textures allows a very precise determination of the P-T evolution of anatectic crustal rocks [23]. In addition, the pseudosection approach has been used to constrain the P-T conditions of metamorphism by comparing the calculated isopleths for mineral composition with the measured compositions [24]. In particular, modeling the effects of melt loss in felsic and pelitic systems [25–28] provides a cadre for the evaluation of the prograde P-T evolution that was previously impossible, because the composition of the rock in which prograde minerals developed has been irrevocably changed [27,28].

In this context, we used microstructures, petrography, mineral chemistry, and phase equilibria modeling to show that the migmatitic paragneisses of the Filali unit were subjected to partial melting into the sillimanite stability field during the Alpine event. In this study, we used melt reintegration modeling to recreate prograde subsolidus bulk rock compositions of residual migmatitic paragneisses. Our goal was to reconstruct and interpret the P-T path to identify the conditions of the Variscan and Alpine metamorphism for the migmatitic paragneisses of the Filali unit. The structural data combined with P-T metamorphic estimates will provide an important key for understanding the tectonometamorphic evolution of the Internal Rif and, in turn, the overall tectonic framework of the internal Alpine orogenic belt in the western Mediterranean area.

2. Geological Setting

The Betic-Rif region is located at the extreme tip of the western Mediterranean Sea and wedged between the Iberian and African plates (Figure 1a). This orogenic chain has a very particular geometry with its arcuate shape. The northern part of this chain, located on the Iberian margin, corresponds to the Betic Cordilleras, while the Moroccan branch corresponds to the Rif chain. The geological evolution of the Rif Mountain range shows striking similarities with the Betics range in Spain (Figure 1b). The Internal domains (Alboran domain) of the Alpine Rif and Betic Cordillera include the Beni Bousera and Ronda subcontinental peridotites, respectively [29]. This orogenic chain shows a complex geological evolution, interpreted as the final consequence of the convergence between Africa and Eurasia accommodated since the Late Cretaceous by the subduction of the oceanic lithosphere [5,6,10].

Three main structural domains are distinguished, from top to bottom, in the Rif belt (Figure 1b) [8]: (i) the External domain, (ii) the Flysch nappes, and (iii) the Internal domain (the Alboran domain). The Alboran domain in the Rif is constituted, from top to bottom, by three major complexes (Figure 1b), the Mesozoic carbonates of the Dorsale units, the Ghomaride, and the Sebtide. The latter two metamorphic complexes have their equivalents in the Betic chain that correspond to the Malaguide and the Alpujarride, respectively (Figure 1b). The lower tectonic complex is the eclogite-bearing Nevado–Filabride complex [30] of the Betic Cordillera that is not exposed in the Rif region (Figure 1b) [11].

The Ghomarides, located at the top of the Sebtides units (Figure 1b), are essentially formed of a pile of low-grade Paleozoic metamorphic formations overlain by non-metamorphic Permo-Triassic sedimentary cover. A gradient temperature is observed from the top of the structural pile, with temperatures of <300 °C, to the top, with temperatures of 550 °C [31].

The Sebtides units consist of a stack of metamorphic rocks that range from high to low grade and are derived from Paleozoic to Triassic protoliths, with thermal contrasts and metamorphic gaps, suggesting that most of their tectonic contacts are brittle extensional detachments. There are two distinct tectonometamorphic complexes in the Sebtides. The first complex is located in the upper position and is associated with the Upper Sebtides (Federico and Beni Mzela units). The second complex is located in the basal position and is associated with the Lower Sebtides, which consist of the Filali, Beni Bousera, and Monte Hacho units, in that order, from top to bottom. At the base of the Lower Sebtides, there is the Beni Bousera unit, characterized by ultramafic bodies at the bottom, overlain by an

aluminous granulite layer. On top of this unit, there are the migmatitic paragneisses, the gneisses, and micaschists belonging to the Filali unit.

The metamorphic evolution from the metapelites of the Filali unit is marked by a polycyclic evolution characterized by an MP-MT Variscan event (ca. 250 Ma through monazite dating) [9]. The peak conditions of the MP-MT event are 550–670 °C and 5–8.5 kbar and correspond to a 20–26 °C/km barrovian-type metamorphic gradient [9]. This event was followed by an LP-HT event equilibrated at 550–750 °C and 3–6 kbar (geothermal gradient of 45 °C/km), Alpine in age at ca. 21 Ma [9]. Recent studies show that the medium-pressure (Barrovian) metamorphism of the Filali unit, related to crustal thickening during the Variscan orogeny, is followed by an Alpine thinning of the continental lithosphere, leading to the exhumation of subcontinental mantle rocks (~22 Ma; U-Pb zircon/monazite and $^{40}Ar/^{39}Ar$ muscovite/biotite) [32]; see also Gueydan et al. [9]. The Filali unit is separated from the underlying Beni Bousera unit by an extensional shear zone [9,33]. The Upper Sebtides Complex (Federico units) consists of Permo-Triassic metasediments; part of these units exhibits mineral associations indicating a high-pressure/low-temperature (HP-LT) metamorphism under blue schist to eclogite facies related to Alpine subduction [34,35].

The granulite overlying the peridotite is mainly composed of metapelite rocks interlayered with minor mafic granulites, the latter occurring as boudins close to the contact with the peridotites [14,16,36–38]. The metamorphic evolution of the granulite rocks indicates an isothermal decompression P-T path, starting at HP/HT conditions of ~800 °C and 12–15 up to 20 kbar [36], 800–870 °C and 10.5–13 kbar [32], or 900–950 °C and 12–14 kbar down to 800–850 °C and 11–13 kbar [14], and ending with a final re-equilibration producing retrograde cordierite–spinel–sillimanite under conditions of 650–750 °C and 4–5 kbar [32,36,37]. The age of the climax of the metamorphism is still debated, considered either Variscan (290–300 Ma) [14] or Alpine (21–22 Ma) [14].

The Beni Bousera and Ronda belong to the groups of high-temperature alpine peridotites of the lherzolitic subtype that border the western Mediterranean [39–41]. These peridotites are located at the base of the Sebtides–Alpujárrides units (Figure 2) [39–41]. In the Beni Bousera peridotite massif, two structural domains are distinguished, a spinel tectonite domain in the core of the massif and a garnet–spinel mylonite domain at the top [33]. Gravimetric data suggest that these peridotite bodies correspond to a few kilometer-thick slices underlain by crustal material, and probably extend offshore [42]. The occurrence of graphite pseudomorphs after diamond, observed in garnet pyroxenites, indicates an ultrahigh-pressure origin of these peridotites ($P > 45$ kbar) for temperatures in the range of 1350–1400 °C and confirms their very deep origin [43–45].

The exhumation and emplacement processes of the Beni Bousera and Ronda peridotite bodies into the continental crust are still strongly debated: (i) a post-collision extensional collapse of the Betic-Rif chain following the convective removal of the lithospheric root [46] or (ii) delamination of the orogenic root [47,48]. Other models have favored thrusting (1) during the Alpine orogeny (Paleogene) [49], following either a Jurassic [50,51] or Variscan exhumation event [12], or (2) during slab roll-back of the Tethyan oceanic lithosphere at ca. 21–23 Ma, following mantle exhumation in a back-arc setting at ca. 25–23 Ma [52]. However, the available radiometric ages (zircon and apatite fission track) constrain the final exhumation of the Ronda and Beni Bousera peridotites during Burdigalian–Langhian times (ca. 19.5–15.5 Ma) [53].

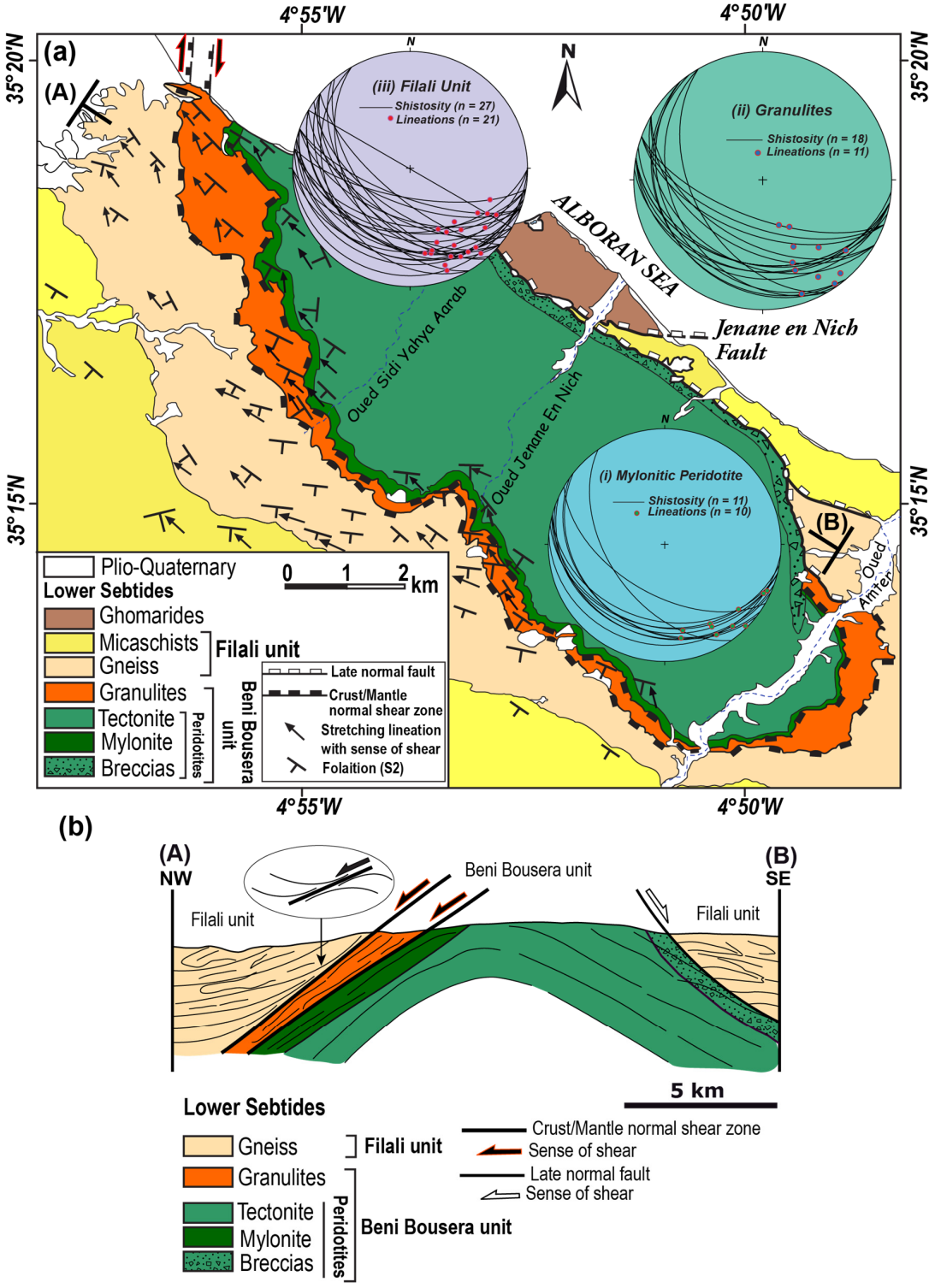

Figure 2. (**a**) Geologic and tectonic map of the studied area (the Beni Bousera peridotites and the overlying crustal rocks: granulite and Filali units) showing the main directions of the S2 foliation and stretching lineation. Foliation data are indicated by black symbols and lineation data are represented by black lines with arrows. The figure shows stereoplots, lower-hemisphere equal-area projections of structural data, of the poles of the plane foliation and lineation in the peridotites (i), in the granulite (ii), and in the Filali unit (iii), modified after Afiri et al. [33], Reuber et al. [40] and El Bakili et al. [54]. (**b**) NW–SE cross-section showing that the contact between the Beni Bousera peridotites and crustal rocks consists of a lithospheric scale extensional shear zone.

3. Materials and Methods

The bulk composition used for the modeling was obtained through the area-scan method of SEM-EDS (Scanning Electron Microscopy and Microanalysis Center, EDAX TEAM, Faculty of Sciences-Semlalia, Caddi Ayyad University, Marrakech, Morocco) on parts of thin sections estimated to approach an equilibration volume. Due to the heterogeneous nature of the samples (the presence of porphyroblasts or layering), the analyses were performed using different surface sizes and the robustness of the results was checked (Table 1). The bulk compositions used are shown as insets in the diagrams in mole percent normalized to 100%.

To characterize the composition and chemical heterogeneities of the minerals, in situ quantitative chemical analyses of the major elements were performed with a CAMECA-SX100 electron microprobe (Microsonde Ouest, IFREMER, Brest-Plouzan, France). The operating conditions for the spot analyses were 15 keV accelerating voltage for 20nA sample current with 20 s counting time on the peak with a beam of micrometric diameter.

Representative analyses of selected mineral phases are listed in Table 2. Mineral abbreviations follow the THERMOCALC terminology—and: andalusite, bi: biotite, cd: cordierite, ep: epidote, g: garnet, ilm: ilmenite, ksp: potassium feldspar, ky: kyanite, mu: muscovite, liq: melt, pa: paragonite, pl: plagioclase, q: quartz, ru: rutile, and sill: sillimanite. Mineral end-members (expressed in mol.%) and compositional variables are—X_{Fe} = Fe/(Fe + Mg); albite, Ab = Na/(Ca + Na + K); anorthite, An = Ca/(Ca + Na + K); orthoclase, Or = K/(Ca + Na + K); almandine, Alm = Fe/(Fe + Mg + Ca + Mn); pyrope, Prp = Mg/(Fe +Mg + Ca + Mn); grossular, Grs = Ca/(Fe + Mg + Ca + Mn); spessartine, Sps = Mn/(Fe + Mg + Ca + Mn); X_{Mg} = Mg/(Mg + Fe + Mn); m(crd) = Mn/(Mg + Fe + Mn); and ilmenite, Ilm = Fe/ (Fe+Mg+Mn).

4. Results

4.1. Structural Evolution

The Filali unit outcrops immediately at the contact with the granulites (Figure 2) and includes sillimanite–biotite micaschists in its lower part and andalusite–muscovite–biotite micaschists in its upper part. Toward the base of the unit, the micaschists are progressively transformed into migmatites. Intercalations of deformed garnet-bearing aplite, pyroxenite, quartzite, metabasic rocks, and leptynite occur within the Filali unit (Figure 3e) [38,39,55]. The contact between the migmatitic paragneisses and the underlying granulitic unit corresponds to the shear zone, with kinematic indicators showing a dominant extensional component towards the NW (Figure 2).

The migmatitic paragneisses of the Filali unit are generally layered. They display an alternation of leucosome and melanosome layers (Figure 3a–d,f) forming a regional NW–SE gneissic foliation (Figure 2). The relative proportion of leucosome and melanosome varies, even at the outcrop scale. In some outcrops, the leucosome is dominant over the melanosome and forms centimetric layers, while in others, the leucosome and the melanosome proportions are similar, and form alternating millimetric to centimetric bands. The mesosome is frequently rare, which indicates a high melting rate and an evolved nature of the migmatitic paragneisses [56]. The migmatitic texture corresponds to veins and felsic segregations that are parallel to the S2 regional foliation. The foliation bears a stretching lineation outlined by biotite and quartz ribbons [55]. It strikes NW–SE to N–S, parallel to that observed in the surrounding units (Figure 2). The S2 regional foliation is more evolved in the zones where deformation is penetrative and at the contacts between the peridotites and the granulites, where it evolves to a mylonitic foliation.

The main schistosity S2 is generally affected by tight sub-isoclinal folds whose axial plane is parallel to S2 (Figure 3c). This indicates that these folds were generated during a progressive deformation contemporaneous with the main foliation S2. The fold hinges are also parallel to the mineral lineation. The observed structures record a non-coaxial deformation marked by the boudinage of quartzo-feldspathic layers and development of S/C shear bands indicating the top to the NW shearing (Figure 3d). The foliation that

strikes N110–140 within the peridotites shows a systematic rotation toward the contact with the granulites, where it becomes parallel to the contact crust and mantle and strikes N170 near the granulites (Figure 2). This progressive rotation of the main foliation trajectories is related to the kilometer-scale top to the NW extensional shear zone, with a dextral component along this crust/mantle contact at the scale of the Lower Sebtides: peridotites, granulites, and Filali unit [9,32,55].

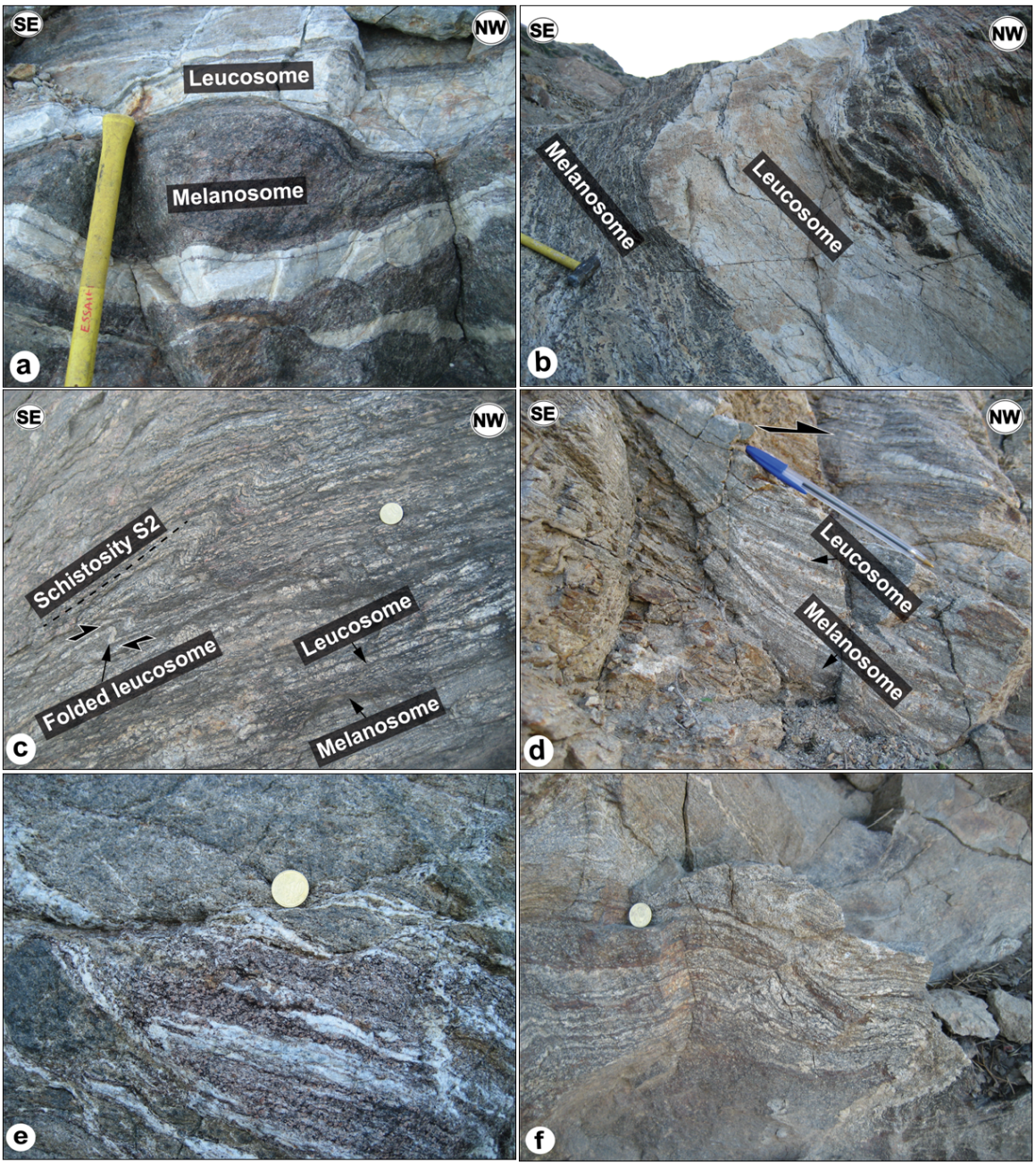

Figure 3. Field photographs showing different geometric relationships between partial melting and main schistosity S2 in the migmatitic paragneisses of the Filali unit. (**a**) Granitic leucosomes parallel to S2 schistosity. (**b**) Aplitic veins oriented parallel to the main schistosity S2. (**c**) Asymmetrical P2 folds overturned to the NW deforming leucosomes. (**d**) Top to the NW shear bands. (**e**) Metabasic levels intercalated in migmatitic paragneisses, boudinaged and surrounded by the main foliation S2. (**f**) Alternating leucosomes and melanosomes; leucosomes are boudinaged, stretched, and parallel to the regional foliation S2.

4.2. Petrology and Mineral Chemistry

The main regional schistosity S2 is generally defined by preferred orientations of fibrolitic sillimanite, and biotite (Figure 4d; X_{Fe} = 0.62–0.66, Al^{VI} = 0.25–0.46, and Ti = 0.21–0.26 apfu) (Table 2), biotite–sillimanite intergrowth and, in minor amounts, ilmenite (Figure 5). The schistosity S2 wraps around rare large crystals of garnet and plagioclase (Figure 4a,f). The leucosomes contain abundant plagioclase and quartz, with minor k-feldspar and local garnet, fibrolite, cordierite, and biotite. The grain size of quartz and k-feldspar is larger than that of other minerals, ranging from one to several millimeters. The melanosomes are composed by the preferred orientation of fibrolitic sillimanite, biotite, plagioclase (Ab_{46-51}, An_{53-48}, and Or_1) (Table 2), and small crystals of garnet (max. 1.5 mm; X_{Fe} = 0.87–0.91, Alm_{73-77}, Prp_{12-7}, Grs_{7-4}, and Sps_{7-11}), as well as ilmenite and quartz. Subhedral garnet crystals (0.2 mm) are commonly surrounded by small clusters of fibrolite (Figure 4c) and cordierite (X_{Fe} = 0.56–0.58). Subhedral crystals of kyanite show undulate extinction, indicating pre-kinematic growth (Figure 4b). Andalusite has an ellipsoidal form that is parallel to, but slightly discordant from, the main schistosity S2. Andalusite porphyroblasts contain inclusions of biotite, plagioclase, quartz, and needles of sillimanite oriented parallel to the S2 schistosity. These microstructural features indicate that andalusite grew late-to post-kinematically to the S2 schistosity (Figure 4e). Muscovite forms small plates arranged oblique to the gneissic foliation in the matrix and as replacement products after andalusite and cordierite. Plagioclase generally forms large (up to 4 mm) crystals and contains inclusions of biotite, kyanite, muscovite, ilmenite, and quartz. Garnet forms large (up to 6 mm) anhedral porphyroblasts that are optically zoned (Figure 4f) and contain inclusions of biotite, rutile, plagioclase, apatite, ilmenite, and quartz. Inclusions are concentrated at the interface core rim of the crystals. In the core (X_{Fe} = 0.91–0.93, Alm_{69-76}, Prp_{8-5}, Sps_{11-19}, and Grs_{7-4}), they define an internal schistosity (S1) oriented at a high angle and discontinuous with the matrix S2. Ilmenite and biotite exclusively preserved as tiny inclusions in the rim are generally parallel or at a low angle to the S2 matrix. These microstructural relationships indicate pre- to syn-S2 garnet growth (Figure 5). Garnet rims (X_{Fe} = 0.87–0.92, Alm_{72-80}, Prp_{12-6}, Sps_{4-12}, and Grs_{8-4}) are generally rich in inclusions (generally biotite and ilmenite) that are oriented parallel to the main schistosity S2 (Figure 4a). The garnet rims are in textural equilibrium with the matrix minerals. This generation of garnets (g2) shows resorbed edges by oriented biotite, k-feldspar, and sillimanite aggregates. These garnet crystals are chemically zoned (Figures 6 and 7).

A large core is characterized by a smooth bell-shaped reward of decreasing content of spessartine (Sps 13→4) and X_{Fe} (X_{Fe} = 0.91→0.87) and increasing content of grossular (Grs 5→8), followed by increasing content of spessartine (Sps 4→10) and X_{Fe} (X_{Fe} = 0.87→0.89) and decreasing content of grossular (Grs 8→5). The rim is marked by contrasting zoning characterized by a flat inner part and zoned outermost rim (Alm 77→78, Prp 14→6, Grs 8→4→6, Sps 2→11, and X_{Fe} = 0.85→0.93). These compositional characteristics are typical of high-grade garnets affected by HT re-equilibration and diffusive re-homogenization during retrogression [57], and small garnet crystals, chemically similar to the rim of the garnet porphyroblasts.

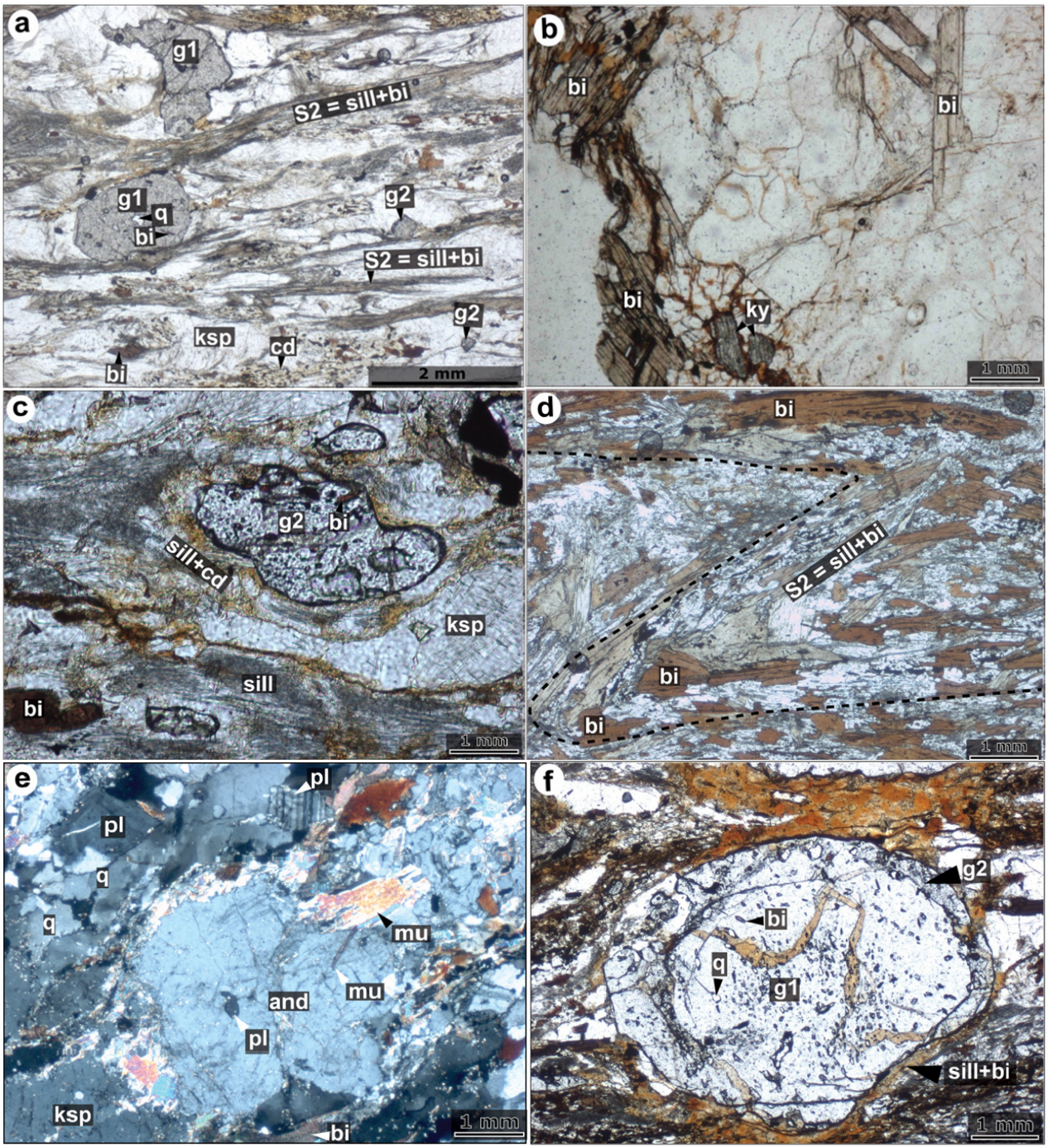

Figure 4. Crystallization/deformation relationships in the migmatitic paragneisses of the Filali unit. (**a**) Two types of garnets are perfectly recognizable: porphyroblasts wrapped by the biotite–sillimanite main schistosity S2 containing inclusion trails of quartz and biotite (S1); small garnets dispersed in a bed of quartz and k-feldspar and slightly wrapped by sillimanite and biotite; garnet porphyroblasts (g1), and garnet with a small size (g2). (**b**) Pre-S2 kyanite porphyroclasts wrapped by the biotite–sillimanite foliation. (**c**) Transformation of a second-generation garnet (g2) into cordierite and sillimanite. (**d**) Foliation S2, defined by biotite and sillimanite, is folded. (**e**) Late-S2 Subhedral andalusite porphyroblast includes plagioclase and muscovite inclusions. (**f**) Garnet shows a core (g1), separated by an optical (and chemical) discontinuity from a peripheral zone (g2). Schistosity S2, composed of sillimanite, biotite, and garnet 2, parallel to thin leucosomes, wraps around large crystals of garnet 1, surrounded by rims of garnet 2.

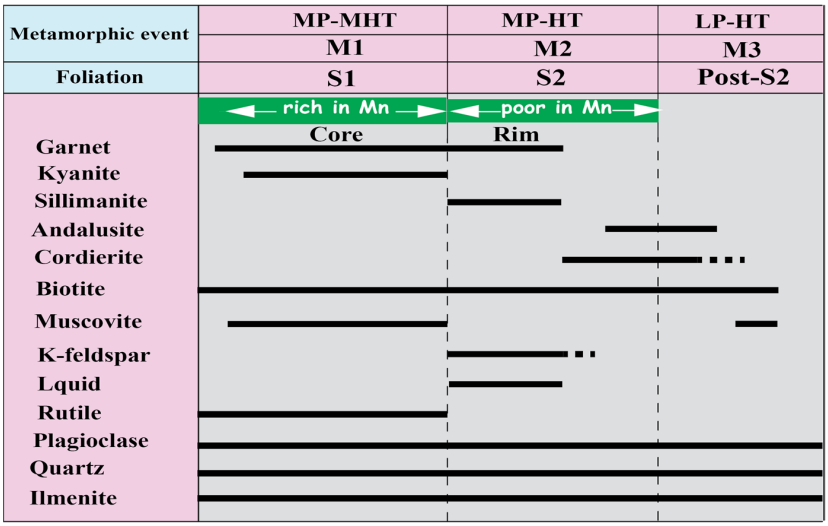

Figure 5. Temporal relationship between metamorphism and deformation in the migmatitic paragneisses of the Filali unit. The figure also shows the main mineralogical assemblages representative of both S1 and S2 schistosities in this rock.

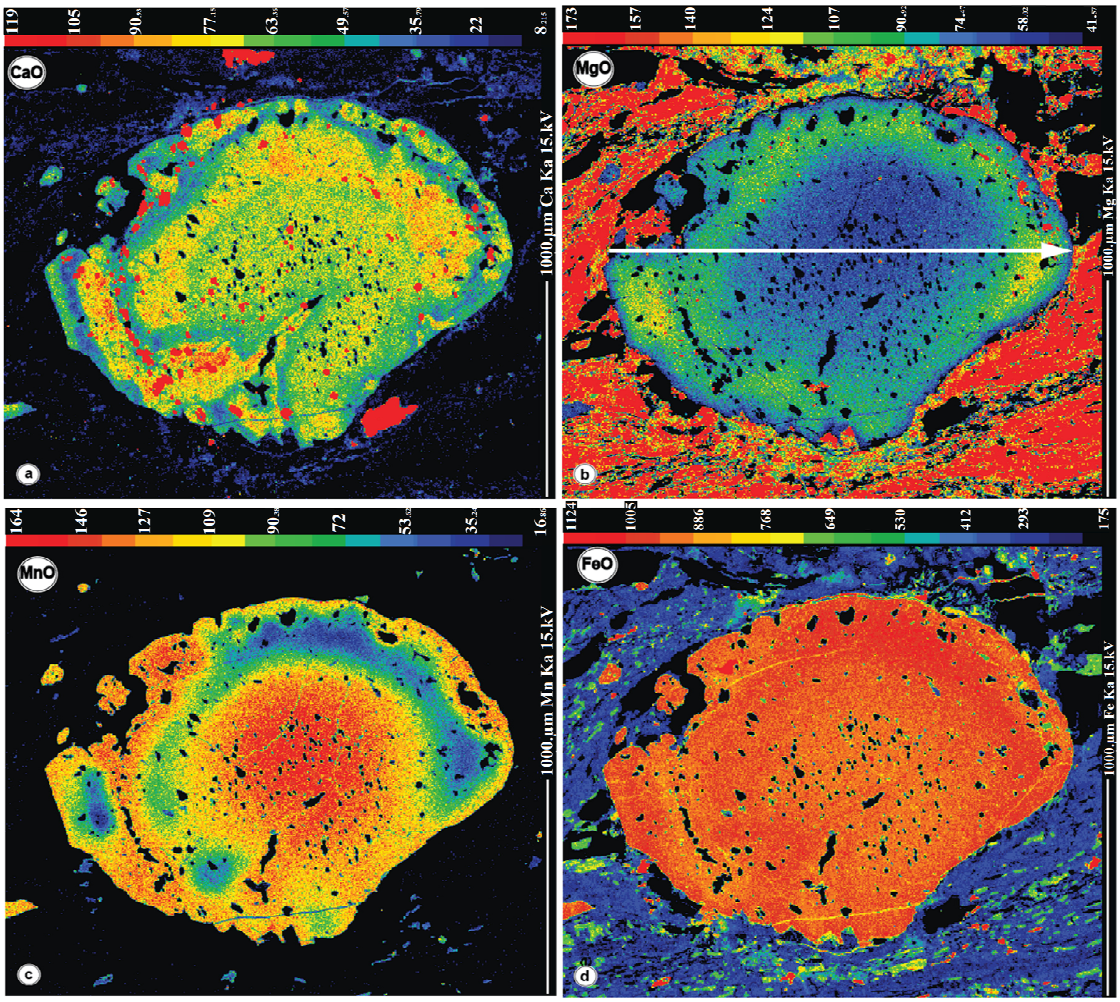

Figure 6. X-ray mapping of garnet from the migmatitic paragneisses of the Filali unit. (**a**) CaO, (**b**) MgO, (**c**) MnO, and (**d**) FeO mapping. Note that the "warm" colors indicate high concentrations and the "cold" colors indicate low concentrations. The white line in (**b**) refers to the location of the garnet compositional profile shown in Figure 7.

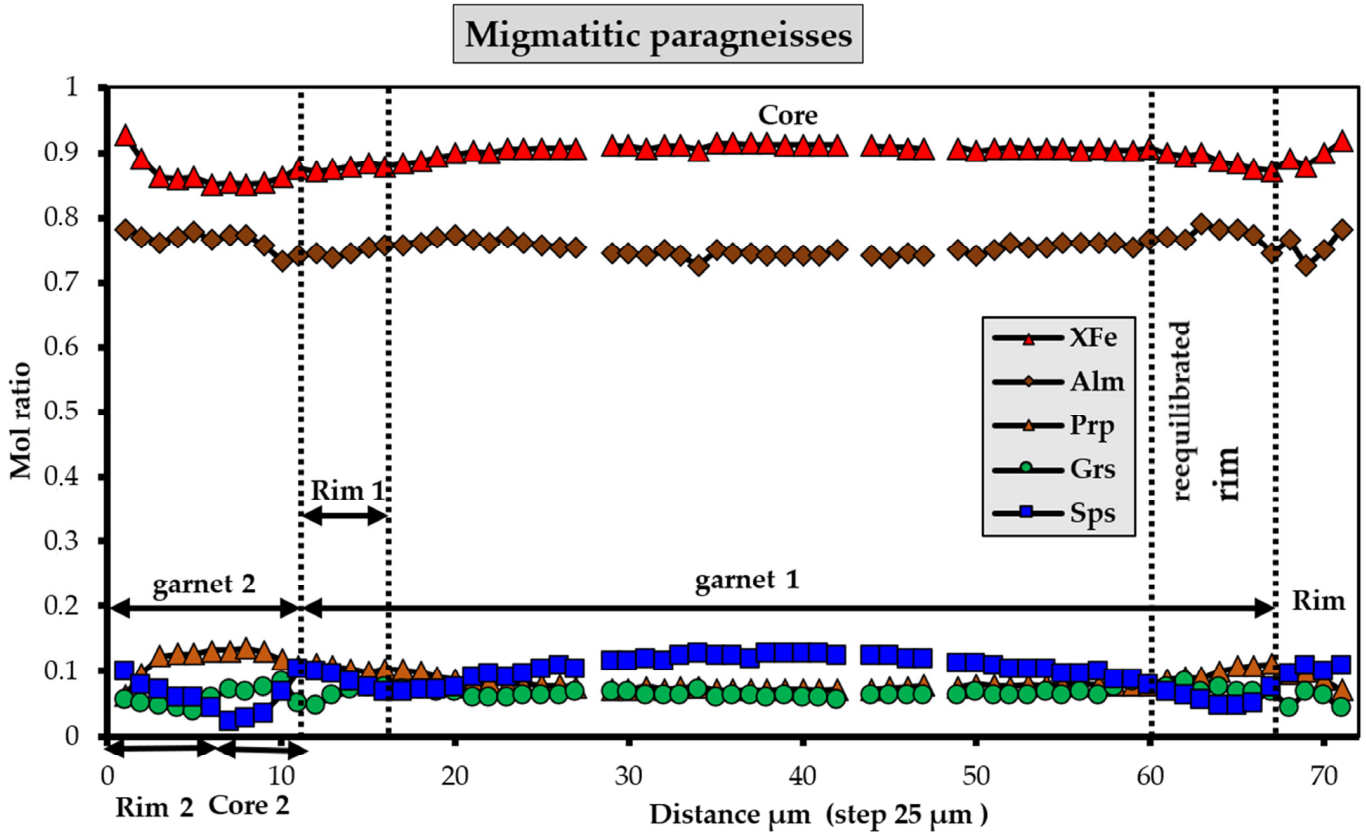

Figure 7. Chemical zoning profile of garnet from the migmatitic paragneisses of the Filali unit.

In summary, it is deduced that three stages are recognized in the metamorphic evolution of the aluminous migmatitic paragneisses, marked by the chemical zoning of garnet porphyroblasts and the evolution of associated mineral assemblages characterized by an early metamorphic peak assemblage containing garnet 1 (core), kyanite, biotite, plagioclase, muscovite, ilmenite, rutile, and quartz (M1), a syn-thermal peak assemblage involving a second generation of garnet 2 (inner rims) that is in equilibrium with sillimanite, biotite, plagioclase, k-feldspar, ilmenite, quartz, and melt (M2), and a retrograde assemblage composed of garnet 2 (outer rims), sillimanite, biotite, plagioclase, k-feldspar, rutile, ilmenite, quartz, and cordierite (M3). The outer parts of both the core and the rim zoning of garnet porphyroblasts, characterized by a significant increase in spessartine, are interpretable as the result of the partial resorption and re-equilibration of garnet during the development of the two schistosities S1 and S2, respectively. This suggests that the paragneisses recorded a polymetamorphic evolution.

4.3. Pseudosections and Thermobarometry

To decipher the tectonic evolution of the migmatitic paragneisses of the Filali unit, we conducted a petrographic study coupled with chemical analyses of minerals and rocks, which allowed us to determine the P-T conditions of these paragneisses.

The P-T pseudosections were calculated in the model system MnNCKFMASHTO using thermocalc and the thermodynamic data set 5.5 (updated November 2003) [58], from the representative composition of the equilibrium minerals of sample BB0618 (Table 1). Thus, P-T calculations of the different mineralogical assemblages for the migmatitic paragneisses of the Filali unit were performed using the multi-equilibrium thermobarometric "average PT" (av. PT) mode [59], and the compositions of minerals were inferred to be in equilibrium. The activities of the mineral end-members were calculated with the program AX [60] in [61]. The results are summarized in Table 3. The solution phases considered in the calculations and the activity–composition models used are white micas [62], plagioclase [63], ilmenite–

hematite [64], and biotite and melt [23]. The mixing models for other solid solutions were based on Holland and Powell [58]. No ideality parameters were from Holland and Powell [58] and the THERMOCALC documentation [61].

Table 1. Bulk rock composition, used for the calculation of the pseudosection in Figure 8, was analyzed (given in Weight %) and converted to the model system MnNCKFMASHTO (in mol.%).

H_2O	SiO_2	Al_2O_3	FeO	MgO	CaO	NaO_2	K_2O	TiO_2	MnO	Fe_2O_3	Total
5.25	59.87	17.05	4.82	5.58	2.05	1.18	2.12	1.09	0.89	0.10	100.00

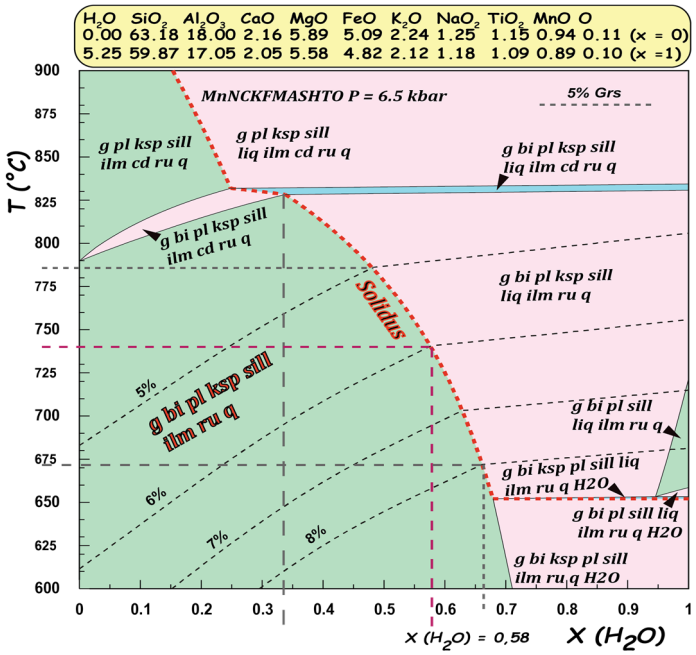

Figure 8. T-X_{H_2O} pseudosection calculated at 6.5 kbar in the MnNCKFMASHTO chemical system, with calculated compositional isopleths of the grossular (Grs) content of garnet used for determining the bulk H_2O content. The observed syn-thermal peak assemblage (g bi pl ksp sill ilm ru q) is stable just above the solidus for X_{H_2O} values ranging from 0.34 to 0.66 mol.%. Red dashed line: solidus. Pink dashed line: selected X_{H_2O} (0.58) value.

Table 2. Representative microprobe analyses of principal metamorphic minerals from the migmatitic paragneisses of the Filali unit. The amount of ferric iron was calculated from stoichiometric constraints using the program AX. Inc = inclusion.

Mineral	g	g	g	g	g	g	g	g	g	bi	bi	bi	cd	cd	pl	pl	pl	ksp	ksp
Analysis No.	604	41	605	215	65	66	67	8	11	209	211	718	504	506	101	102	301	104	105
Position	g1 core	g1 core	g1 core	g1 core	g1 rim	g1 rim	g1 rim	g2 core	g2 rim	matrix	matrix	bi inc-g	matrix	matrix	matrix	matrix	matrix	matrix	matrix
SiO_2	36.9	37.31	36.96	37.19	37.40	37.64	37.67	37.59	37.48	34.6	34.65	34.52	47.44	47.74	54.7	55.22	55.16	64.62	64.93
TiO_2	0.08	0.01	0.03	0.07	0.04	0.10	0.00	0.04	0.02	4.31	4.01	3.98	0.00	0.07	0.04	0.04	0.04	0.01	0.05
Al2O3	20.61	20.54	20.92	20.79	20.56	20.53	20.90	21.10	20.49	19.73	19.40	17.74	32.52	32.53	28.53	28.67	28.01	18.93	18.83
Cr_2O_3	0.00	0.06	0.02	0.04	0.02	0.02	0.02	0.07	0.00	0.03	0.04	0.01	0.08	0.04	0.08	0.01	0.02	0.01	0.03
Fe_2O_3	0.25	0.00	0.00	0.00	0.33	0.00	0.00	0.62	0.15	0.06	0.05	0.00							
MgO	1.53	1.76	1.43	1.45	2.49	2.63	2.73	3.41	2.65	6.36	6.43	7.39	5.13	5.08	0.02	0.00	0.00	0.00	0.01
FeO	31.2	32.59	31.53	30.47	34.89	34.82	34.62	34.67	33.24	21.97	20.93	21.94	12.49	12.56	0.08	0.09	0.08	0.11	0.07
MnO	6.96	5.49	7.24	8.13	1.97	2.02	2.24	1.11	4.52	0.16	0.14	0.21	0.47	0.47	0.01	0.01	0.03	0.07	0.02
CaO	2.02	2.01	1.99	2.41	2.55	2.37	2.39	2.36	1.80	0.03	0.25	0.11	0.03	0.03	10.86	10.81	10.76	0.07	0.01
P_2O_5	0.05	0.12	0.09	0.18	0.02	0.05	0.05	0.02	0.05	0.01	0.02	0.03	0.01	0.02	0.03	0.00	0.05	0.07	0.03
Na_2O	0.13	0.03	0.04	0.06	0.02	0.01	0.02	0.02	0.01	0.12	0.12	0.25	0.29	0.21	5.27	5.58	5.62	1.67	1.80
K_2O	0.01	0.03	0.02	0.01	0.04	0.00	0.02	0.01	0.01	9.97	8.81	8.60	0.00	0.00	0.15	0.20	0.15	14.61	15.12
H_2O										3.95	3.89	3.86							
Sum	99.81	99.97	100.35	100.8	100.33	100.19	100.66	101.02	100.43	101.31	98.74	98.63	98.50	98.82	99.79	100.66	100.03	100.18	100.96
Si	3.00	3.03	2.99	2.99	3.01	3.03	3.02	2.99	3.02	2.62	2.67	2.68	4.98	5.00	2.47	2.48	2.49	2.97	2.97
Ti	0.00	0.00	0.00	0.00	0.00	0.01	0.00	0.00	0.00	0.25	0.23	0.23	0.00	0.01	0.00	0.00	0.00	0.00	0.00
Al	1.97	1.96	1.99	1.97	1.95	1.95	1.97	1.98	1.95	1.76	1.76	1.62	4.03	4.01	1.52	1.52	1.49	1.03	1.02
Cr	0.01	0.00	0.00	0.00	0.00	0.00	0.00	0.00	0.00	0.00	0.00	0.00	0.01	0.00	0.00	0.00	0.00	0.00	0.00
Fe3	0.00	0.00	0.00	0.00	0.02	0.00	0.00	0.04	0.01	0.00	0.00	0.00							
Mg	0.18	0.21	0.17	0.17	0.30	0.32	0.33	0.40	0.32	0.72	0.74	0.85	0.80	0.79	0.00	0.00	0.00	0.00	0.00
Fe2	2.12	2.21	2.13	2.05	2.35	2.34	2.32	2.31	2.24	1.39	1.35	1.42	1.10	1.10	0.00	0.00	0.00	0.00	0.00
Mn	0.48	0.38	0.49	0.55	0.14	0.14	0.15	0.08	0.31	0.01	0.01	0.01	0.04	0.04	0.00	0.00	0.00	0.00	0.00
Ca	0.17	0.18	0.17	0.20	0.22	0.20	0.21	0.20	0.16	0.00	0.02	0.01	0.00	0.00	0.53	0.52	0.52	0.00	0.00
P	0.00	0.01	0.00	0.01	0.00	0.00	0.00	0.00	0.00	0.00	0.00	0.00	0.00	0.00	0.00	0.00	0.00	0.00	0.00

Table 2. *Cont.*

Mineral	g	g	g	g	g	g	g	g	g	bi	bi	bi	cd	cd	pl	pl	pl	ksp	ksp
Na	0.02	0.01	0.00	0.00	0.00	0.00	0.00	0.00	0.00	0.02	0.02	0.04	0.06	0.04	0.46	0.49	0.49	0.15	0.16
K	0.00	0.00	0.00	0.00	0.00	0.00	0.00	0.00	0.00	0.96	0.86	0.85	0.00	0.00	0.01	0.01	0.01	0.86	0.88
OH										2.00	2.00	2.00							
Sum	8.00	7.98	7.99	7.99	8.00	7.99	8.00	8.00	8.00	9.74	9.66	9.72	11.03	11.01	5.00	5.01	5.01	5.02	5.04
XFe/Xna	0.92	0.91	0.93	0.92	0.89	0.88	0.88	0.85	0.88	0.66	0.65	0.62	0.56	0.57	0.53	0.51	0.51	0.00	0.00
Alm/An	0.72	0.74	0.72	0.69	0.78	0.78	0.77	0.77	0.74						0.46	0.48	0.48	0.15	0.15
Prp/Ab	0.06	0.07	0.06	0.06	0.10	0.11	0.11	0.14	0.11						0.01	0.01	0.01	0.85	0.85
Grs/Or	0.06	0.06	0.06	0.07	0.07	0.07	0.07	0.07	0.05										
Sps	0.16	0.13	0.17	0.19	0.04	0.05	0.05	0.03	0.10										

Table 3. Summary of the results of the average P-T calculations (values in bold) of an early metamorphic peak, syn-thermal peak, and retrograde mineral assemblages of the migmatitic paragneisses of the Filali unit [a].

	Sample Migmatitic Paragneisses					
Assemblage	**Early Metamorphic Peak Assemblage**		**Syn-Thermal Peak Assemblage**		**Retrograde Assemblage**	
End-Member	***a* SD(a)/a**		***a* SD(a)/a**		***a* SD(a)/a**	
Garnet						
Py	0.00270	0.66	0.0022	0.68	0.00038	0.00029
Gr	0.00520	0.61	0.00044	0.76	0.00033	0.00025
Alm	0.36	0.15	0.39	0.15	0.36	0.05
Spss	0.000014	0.000005	0.00091	0.00033	0.0053	0.01
K-felspar						
San			0.86	0.05	0.84	0.04
Ab			0.53	0.06	0.62	0.03
Biotite						
Phl	0.012	0.47	0.016	0.45	0.018	0.0083
Ann	0.073	0.30	0.069	0.31	0.076	0.02
East	0.02	0.44	0.02	0.42	0.02	0.0092
Ilmenite						
Ilm	0.91	0.05	0.91	0.04	0.91	0.04
Pnt	0.041	0.0078	0.024	0.005	0.024	0.005
Geik	0.0056	0.002	0.017	0.0038	0.017	0.0038
Plagioclase						
An	0.70	0.05	0.70	0.05	0.70	0.03
Ab	0.51	0.07	0.51	0.15	0.51	0.03
Cordierite						
Crd					0.23	0.16
Fcrd					0.30	0.14
Mncrd					0.00059	0.75
Muscovite						
Mu	0.78	0.10				
Cel	0.018	0.55				
Fcel	0.020	0.50				
Other	ky, ru, q, H_2O		sill, ru, q, H_2O		still, ru, q, H_2O	
Results		SD		SD		SD
T (°C)	**673**	**55**	**752**	**48**	**703**	**48**
P (kbar)	**8.8**	**0.9**	**8.0**	**0.9**	**3.5**	**0.7**
Correlation	0.726	(1.45)	0.556	(1.45)	0.856	(1.49)
fit	0.91		0.90		1.08	
N(R)	8		5		8	

[a] N(R) = number of independent reactions used. Abbreviations are those used by THERMOCALC. The value of "fit" must be lower than the number that follows in parentheses.

4.4. Phase Equilibria Modeling and P-T Path

The partial melting of the gneisses took place during the second tectonometamorphic event (M2). The available quantity of H_2O plays a major role in phase relations involving silicate fluid. In the present case, this amount was estimated from a T-X pseudosection (Figure 8), where X is the H_2O content in the rock composition, using the presence of the observed assemblage at the solidus as a constraint.

We explored the effect of the amount of H_2O on the topology of the diagram (Figure 8). The T-XH_2O pseudosection was calculated at 6.5 kbar, an average value estimated from the metamorphic conditions of neighboring units (high-grade Filali micaschists and Beni Bousera granulites) in the MnNCKFMASHTO chemical system for determining the bulk H_2O content.

The observed syn-thermal peak assemblage garnet 2 (inner rims)–biotite–sillimanite–plagioclase–k-feldspar–rutile–ilmenite–quartz is stable just above the solidus for X_{H_2O} values ranging from 0.34 to 0.66 mol.% ($0.34 < X_{H_2O} < 0.66$). To estimate more precisely the temperatures of the transition to solidus and the H_2O content of the rock, we calculated the compositional isopleths of the grossular in garnet. At the solidus, the model predicts compositions (Grs0.05-0.08) that correspond to an X_{H_2O} of 0.58 within a temperature range of 670–790 °C (Figure 8). This value was then used to recalculate the P-T pseudosection (Figure 9) in the MnNCKFMASHTO chemical system and using the bulk composition of sample BB0618 of the migmatitic paragneisses obtained from the T–X_{H_2O} diagram (Figure 8): H_2O = 3.68, SiO_2 = 60.86, CaO = 2.08, MgO = 5.67, FeO = 4.90, K_2O = 2.16, NaO_2 = 1.20, TiO_2 = 1.11, MnO = 0.90, and Fe_2O_3(O) = 0.10, with a fixed H_2O content (Figure 9).

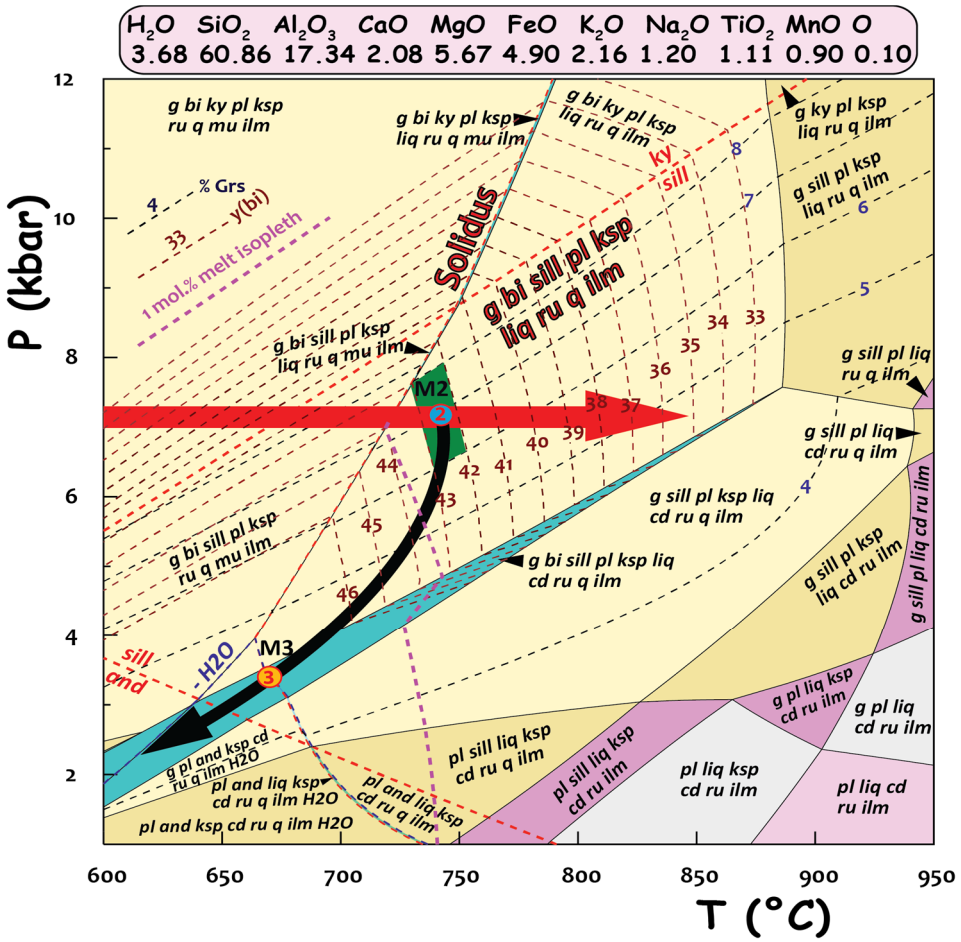

Figure 9. P-T pseudosection calculated using the MnNCKFMASHTO chemical system with the measured bulk composition (SEM-EDS) of migmatitic paragneisses with the proposed prograde P-T path (the red line with arrow). The red thick dashed line is the solidus; the blue, brown, and pink thin dashed lines correspond to the isopleths of the grossular (Grs) content of garnet, the y(bi) in biotite, and melt, respectively. The red bold fonts refer to the observed syn-thermal peak mineral assemblage. The semitransparent blue and yellow circles marked by numbers refer to the syn-thermal peak and retrograde metamorphic P-T conditions constrained by the observed mineral assemblages and the mineral composition isopleths. The black full line with an arrow represents the P-T path of the rock. See text for further details.

4.4.1. Pseudosection Calculated with the Measured Bulk Composition

The pseudosection in Figure 9 is modeled from 600–950 °C and 1–12 kbar. The calculated compositional isopleths of the grossular (Grs) and y(bi) (Al^{VI} = octahedral Al in phyllosilicates = atomic Al+Si − 4) contents of garnet and biotite, respectively, are also

shown in Figure 9. The solidus and the appearance of the anatectic liquid of the system start from temperatures of 670 °C at lower pressures and from 780 °C at higher pressures. Plagioclase, rutile, and ilmenite are always present. Cordierite appears below 7 kbar and garnet disappears below 2 kbar. Muscovite disappears at ca. 600–750 °C above ca. 2.5 kbar, and biotite disappears at ca. 600–850 °C below 2.5 and 7 kbar. The syn-thermal peak and retrograde metamorphic P-T conditions are determined by the position of the stability field of their corresponding respective assemblages on the pseudosection. The observed syn-thermal peak assemblage g2 (inner rims) + sill + bi + pl + ksp+ ru + ilm + q is stable in the P-T field of ca. 3.5–11.5 kbar and ca. 670–890 °C in the presence of melt; the retrograde assemblage g2 (outer rims) + sill + bi + pl + ksp + q + ru + ilm + cd is stable in the P-T range of 640–690 °C and 2.8–3.7 kbar in the absence of melt. This assemblage is stable at the solidus at ca. 685 °C and 3.5 kbar (the yellow-filled red circle in Figure 9).

In upper amphibolite and granulite facies migmatites, pseudosections most often predict the evolution of the P-T conditions of the thermal peak and part of the retrograde path. Certain isopleths of the mineral composition allowed us to calculate the equilibrium P-T conditions of the syn-thermal peak assemblage and to reconstruct the P-T path followed by the rock (Figure 9). The isopleths used are those of the garnet rims (Grs6-8) and matrix biotite (y(bi)42-43). The isopleths corresponding to the composition of the inner rims of garnet (Grs6-8) and biotite (y(bi)42-43) intersect at ca. 750 °C and ca. 7 kbar (the blue circle in Figure 9). The obtained P-T conditions occurred in the stability field of the syn-thermal peak assemblage. Under these conditions, the calculated compositions of garnet rims (Grs6-8) and biotite (y(bi)42-43) agree with those predicted by the phase relationships in Figure 9.

4.4.2. Pseudosection Calculated with the Melt-Reintegrated Bulk Composition

Migmatitic paragneisses have a residual composition after a loss of part of the melt from the partial melting under metamorphic peak conditions. The calculation of the pseudosection by the measured composition thus allows the calculation of only syn and post-thermal peak P-T conditions. For an accurate assessment of the prograde P-T conditions before partial melting, the lost melt must be reintegrated into the bulk composition. The down-temperature melt reintegration approach of Korhonen et al. [65] was applied to reconstruct a plausible protolith bulk composition to model the prograde phase relations.

The melt integration was performed in the stability field where the peak metamorphic assemblage g2 (outer rims) + sill + ksp + bi + pl + q + ru + ilm + melt was observed at >3.5 kbar and >670 °C (Figure 9). The precise P-T location of the melt integration step is not critical as the melt composition does not vary significantly within this stability field [65]. The melt composition was calculated at the intersection point of the proposed prograde P-T path with 1 mol.% isopleth melt at 6.8 kbar and 720 °C. This composition is used for the first melt reintegration step and corresponds to the amount of melt that would be retained as thin films along grain boundaries after melt loss [66]. At this point, 6 mol.% melt was added to the bulk composition to reach a value of 7 mol.% melt in the rock. This volume of melt is analogous to the maximum threshold for melt interconnection and transfer based on experimentally constrained observations of the melt connectivity transition [67]. The prograde P-T path proposed was obtained by the thermobarometric study of the metamorphic barrovian sequence of the Filali unit, including the migmatitic paragneisses (Figure 9) [9,38,55]. One melt reintegration step, corresponding to 6 mol.% melt, was needed to produce a probable protolith bulk composition. The composition of the rock after the reintegration of 6 mol.% melt to the measured composition is: H_2O = 6.30; SiO_2 = 60.90; Al_2O_3 = 16.10; CaO = 1.88; MgO = 5.00; FeO = 4.32; K_2O = 2.29; NaO_2 = 1.36; TiO_2 = 0.98; MnO = 0.79; and Fe_2O_3 = 0.09. This new composition obtained was used to calculate another P-T pseudosection, which showed a water-saturated solidus at 650–675 °C (Figure 10).

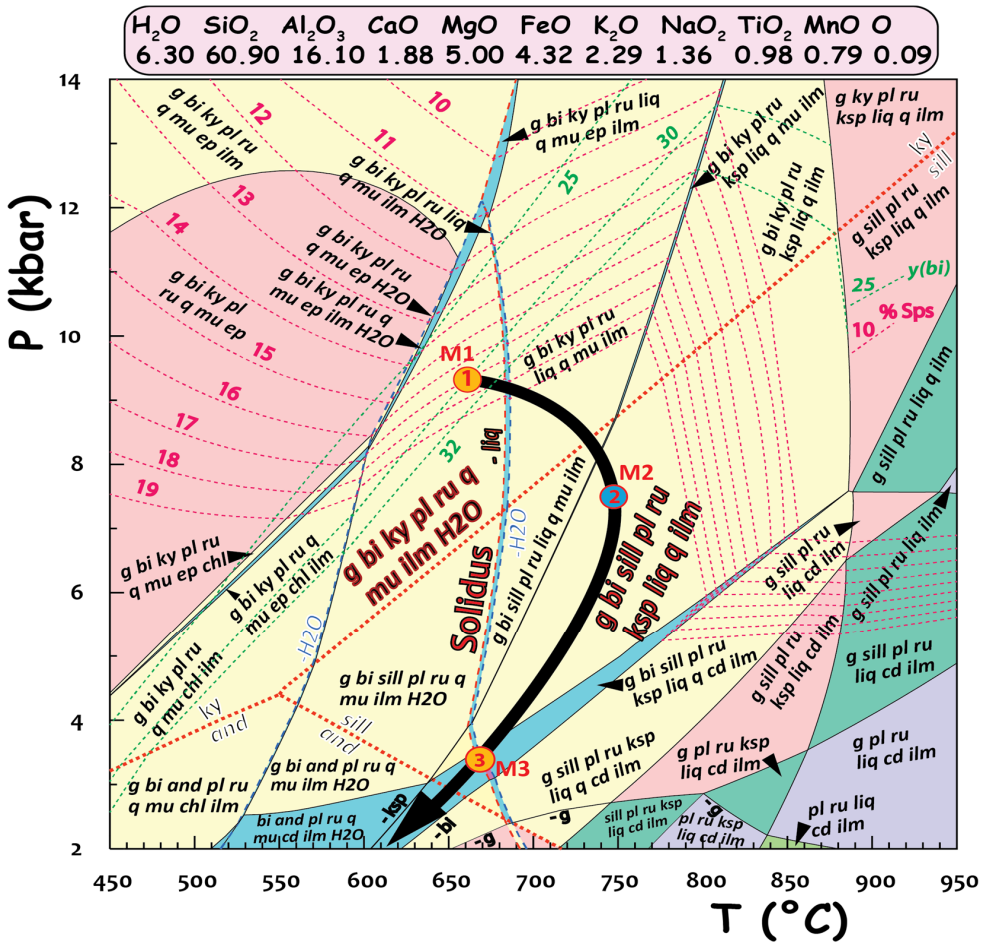

Figure 10. P-T pseudosection constructed in the MnNCKFMASHTO chemical system using the software THERMOCALC, with the melt-reintegrated bulk compositions with 6 mol.% added melt. The blue dashed line is the H_2O-saturated solidus. The red bold fonts refer to the observed early metamorphic peak and syn-thermal peak mineral assemblages. The bulk composition (in mol.%) was calculated with the addition of 6 mol.% melt into the original migmatitic paragneisses composition (Figure 9) and is given above the pseudosection. The dashed bold red line represents the solidus. The red and green dashed lines represent isopleths of the spessartine (Sps) content of garnet and y(bi) in biotite, respectively. The semitransparent blue and yellow circles, marked with numbers 1, 2, and 3, refer to the P-T conditions of the early metamorphic peak, syn-thermal peak, and retrograde assemblages, respectively, constrained by the composition isopleths of garnet and biotite. See text for further details.

Figure 10 shows the P-T pseudosection calculated with the melt-reintegrated bulk composition with 6 mol.% melt for a P-T range of 2–14 kbar and 450–950 °C. When comparing the pseudosection in Figure 10 with that in Figure 9, the topologies at temperatures above the solidus are broadly similar. In contrast, the topologies are drastically different at temperatures below the solidus. The new solidus obtained following the reintegration of 6 mol.% melt is commonly situated below 700 °C, muscovite disappears at ca. 750 °C, and garnet disappears under low-pressure conditions. The observed early metamorphic peak assemblage g1 (core) + ky + bi + mu + pl + q + ru + ilm is stable in the P-T field of ca. 5–12 kbar and ca. 570–675 °C (Figure 10). The measured composition of the garnet (Sps) and biotite (Al^{VI}) isopleths allowed us to estimate the crystallization conditions of the garnet core. The intersection of the relevant compositional isopleths of the garnet core (Sps17-18) and biotite located in the core of garnet (Al^{VI} 30-32) indicates equilibration conditions at 660 °C and 9.3 kbar (the yellow circle 1 in Figure 10). The obtained P-T conditions are located precisely in the stability field of the early metamorphic peak assemblage (M1) g1 (core)-bi-ky-pl-ru-mu-q-ilm (Figure 10).

4.5. P-T Conditions by Using a Multi-Equilibrium Geothermobarometry Approach

The results of average P-T calculations obtained by the multi-equilibrium geothermobarometry approach (av. PT) [59] on the mineralogical assemblages of the migmatitic paragneisses of the Filali unit and the activity models used for the different minerals are summarized in Table 3. Uncertainties represent 1σ value (95% confidence level) on "average PT" results, as calculated by THERMOCALC.

The calculated P-T conditions for the early metamorphic peak assemblage garnet1 (core)–biotite–kyanite–rutile–muscovite–plagioclase–ilmenite are in the order of 673 ± 55 °C and 8.8 ± 0.9 kbar. The PT conditions of syn-thermal peak assemblage garnet 2 (inner rims)–sillimanite–biotite–plagioclase–k-feldspar–rutile–ilmenite are estimated to be around 8.0 ± 0.9 kbar and 752 ± 48 °C. The P-T conditions of the retrograde assemblage garnet 2 (outer rims)–sillimanite–biotite–plagioclase–k-feldspar–cordierite–ilmenite are about 703 ± 48 °C and 3.5 ± 0.7 kbar. These estimates of the early metamorphic peak, syn-thermal peak, and retrograde assemblages are consistent with the results of the approach that is based on phase diagrams (Figures 9 and 10).

5. Discussion

5.1. P-T Evolution of the Migmatitic Paragneisses of the Filali Unit

Three tectonometamorphic events, M1, M2, and M3, are recorded by the migmatitic paragneisses of the Filali unit.

The Variscan M1 event consists of the pre-metamorphic peak assemblage kyanite + biotite + muscovite + plagioclase + rutile + quartz (S1 schistosity) preserved as oriented mineral inclusions (Si) in the cores of garnet 1. Some of these phases may exist in the matrix, where they recrystallize during the following medium-pressure (MP) metamorphic stage. The PT conditions of M1 assemblage are estimated to be around 9.3 kbar and 660 °C (Figure 10) and correspond to a 20 °C/km barrovian-type metamorphic gradient. The Pmax value reached by the migmatitic paragneisses at this stage indicates a burial depth of about 34 km, suggesting a thickening process induced by continental Variscan collision [68].

Monazite U-Th-Pb dating of M1 metamorphic assemblage yielded an age of 170–250 Ma [9]. Variscan U-Th-Pb ages (284 ± 27, 286 − 264, and 294 ± 27 Ma) were also obtained on monazite and zircon grains included in the cores of garnet porphyroblasts of the migmatitic granulites (Kinzigites) of the Beni Bousera Massif [12,14,16]. Similar ages of 281 ± 3 were obtained by El Bakili [18] from the same granulites. In the Betic Cordilleras, U-Pb SHRIMP dating of zircon cores of granulites yielded the same Variscan age of 297 ± 17 Ma [69]. An age of 287 ± 9 Ma was obtained on a monazite inclusion in a garnet core from the migmatitic gneisses of the Jubrique unit equilibrated under granulite–facies conditions [15]. SHRIMP zircon U/Pb dating of the granulite event recorded by the same unit yielded an age of 330 ± 9 Ma corresponding to the Variscan metamorphism [70]. Based on these radiometric data, it seems that the Lower Sebtides–Alpujarrides units underwent a common continental collisional event during the Upper Carboniferous–Lower Permian, as suggested by Michard et al. [71], Bouybaouène et al. [35], Zeck and Whitehouse [72], Whitehouse and Platt [73], Afiri [55], and Gueydan et al. [9].

During its Alpine tectonometamorphic evolution, the migmatitic paragneisses recorded two metamorphic stages, M2 and M3, corresponding to MP-HT and LP-HT events, respectively. The M2 event is coeval with P2 folding and S2 axial-planar regional foliation. This is a syn-metamorphic peak event giving rise to the partial melting of the gneiss during D2 deformation. Their syn-D2 mineral assemblage consists of garnet 2 (inner edges) + sillimanite + biotite + plagioclase + k-feldspar + rutile + ilmenite + quartz + melt. The occurrence of garnet and k-feldspar in the leucosome with evidence of partial melting in the sillimanite stability field suggests the following reaction, which involves the decomposition of an anhydrous mineral, i.e., biotite, in the presence of sillimanite to produce garnet 2, k-feldspar, and an anatectic liquid:

$$\text{Biotite} + \text{Sillimanite} + \text{Quartz} \rightarrow \text{Garnet} + \text{k-feldspar} + \text{Melt} \quad (1)$$

The M2 event resulted from syn-D2 metamorphic decompression, allowing the gneiss to reach thermal peak conditions at 7 kbar and 750 °C. This metamorphic stage occurred in the upper part of the granulite facies in response to a thermal gradient of 30 °C/km.

The subsequent retrograde M3 event is characterized by the occurrence of garnet 2 (outer rim) + sillimanite + biotite + plagioclase + k-feldspar + cordierite + rutile + ilmenite + quartz. In the leucosomes, relics of garnets 2 are intensely resorbed and replaced by aggregates of biotite and sillimanite in the presence of k-feldspar, suggesting that prograde reaction 1 occurred in the opposite direction during retrograde metamorphic evolution under relatively low pressure.

Furthermore, the occurrence of cordierite, including fibrolitic sillimanite, in the leucosomes suggests the following reaction:

$$\text{Garnet} + \text{Sillimanite} + \text{Quartz} + H_2O \rightarrow \text{Cordierite} \quad (2)$$

The PT conditions of the retrograde assemblage (M3 event) were estimated to be around 3.5 kbar and 685 °C. This LP-HT event occurred in the amphibolite facies in response to a sequence of decompressive reactions along a sub-isothermal P-T path (Figure 11) during the exhumation of migmatitic paragneisses. The sub-isothermal decompression was followed by a quasi-isobaric cooling that occurred in the andalusite stability field (green schist facies; 2–4 kbar and 520–630 °C). Similar isothermal decompression has been documented in other units of the Lower Sebtides (Figure 12), whose tectonic boundaries are characterized by significant metamorphic gaps, suggesting their extensional nature. These extensional detachments are at the origin of the exhumation of the different units of the Lower Sebtides–Alpujarrides Complex [33,36,70] at the Oligo-Miocene [9,55,74,75] in a back-arc extensional context linked to a westward retreat of the Alpine subduction [76].

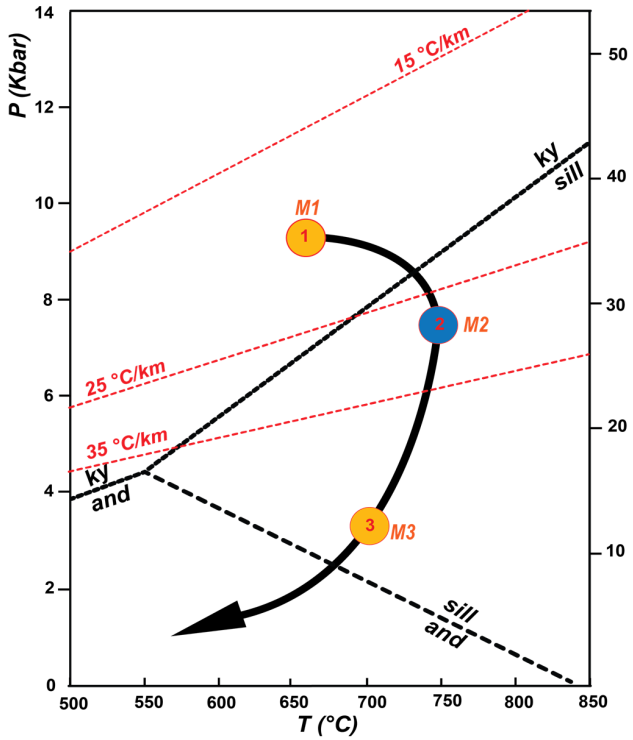

Figure 11. Metamorphic P-T path of the migmatitic paragneisses of the Filali unit. The P-T conditions demonstrate that the migmatitic paragneisses underwent three major tectonic metamorphic events, MP-MHT (M1), MP-HT (M2), and LP-HT (M3). The semitransparent circles, marked with numbers, refer to the P-T conditions of the early metamorphic peak, syn-thermal peak, and retrograde assemblages. The obtained retrograde path suggests a clockwise P-T path and a sub-isothermal decompression followed by cooling. See text for further details.

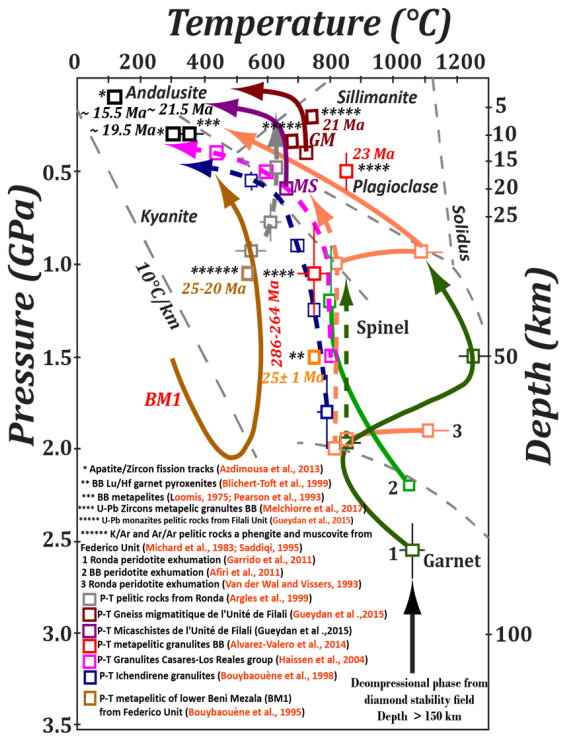

Figure 12. Summary diagram of the different pressure–temperature–time (P-T-t) paths, as well as geochronological data, of peridotite emplacement, tectonometamorphic events of the entire Alboran domain units in Beni Bousera (BB), and Ronda, modified from Melchiorre et al. [16].

5.2. Geodynamic Implications

Our study, together with previous studies, shows that the high-grade crustal units of the Internal domain (the Alboran domain) of the Betic-Rif chain underwent a polymetamorphic evolution, which began already during the Variscan orogeny and continued during the Alpine one [14,77,78]. The particularity of the Betic-Rif chain resides in the exhumation of mantle-derived peridotite bodies into the crust. The presumed ages of the peridotites emplacement are still debated among (i) Paleozoic e.g., [14,79,80], (ii) Mesozoic e.g., [50,81], and (iii) Oligo-Miocene e.g., [9,32,82]. However, the inferred scenario for the emplacement of peridotites was based on the study of P-T-t paths in various polymetamorphic environments. These studies were coupled with tectonic/geodynamic reconstructions of the tectonic coupling between peridotites and crustal rocks of the Betic-Rif arc in the context of the geodynamics of the western Mediterranean e.g., [9,14,16,46,52,83–87].

The proposed geodynamic model (Figure 13) shows that, during the late Carboniferous and Permian [14,16], the Variscan orogeny led to significant crustal thickening, which was responsible for HP-HT metamorphism in the Beni Bousera granulites [12,14,16] and MP-MHT metamorphism in the migmatitic paragneisses of the Filali unit (Figure 13a). This crustal thickening resulted from the convergence between Laurasia and Gondwana [88]. After the extensional collapse that followed the Variscan orogeny [10,14,16,35,71], the post-Variscan crust constituted of granulite, paragneisses, gneiss, and Palaeozoic micaschists became the basement of the Mesozoic sediments deposited at the Tethyan margin [8]. This episode of early Mesozoic lithospheric thinning, contemporary with the opening of the Tethys Ocean, is related to the Lower Jurassic breakup of Pangea in an extensional context [16]. Crustal thinning resulting from the upwelling of the asthenospheric mantle would be responsible for the exhumation of the Beni Bousera peridotite from the diamond stability field (depth > 150 km) to depths of 80 to 100 km i.e., at the lower lithosphere boundary (Figure 13b) [32,50,89]. Other hypotheses have suggested that hyper-thinning led to the exhumation of these mantle rocks to shallow depths on the margins of the Maghrebian Tethys since the Triassic [81].

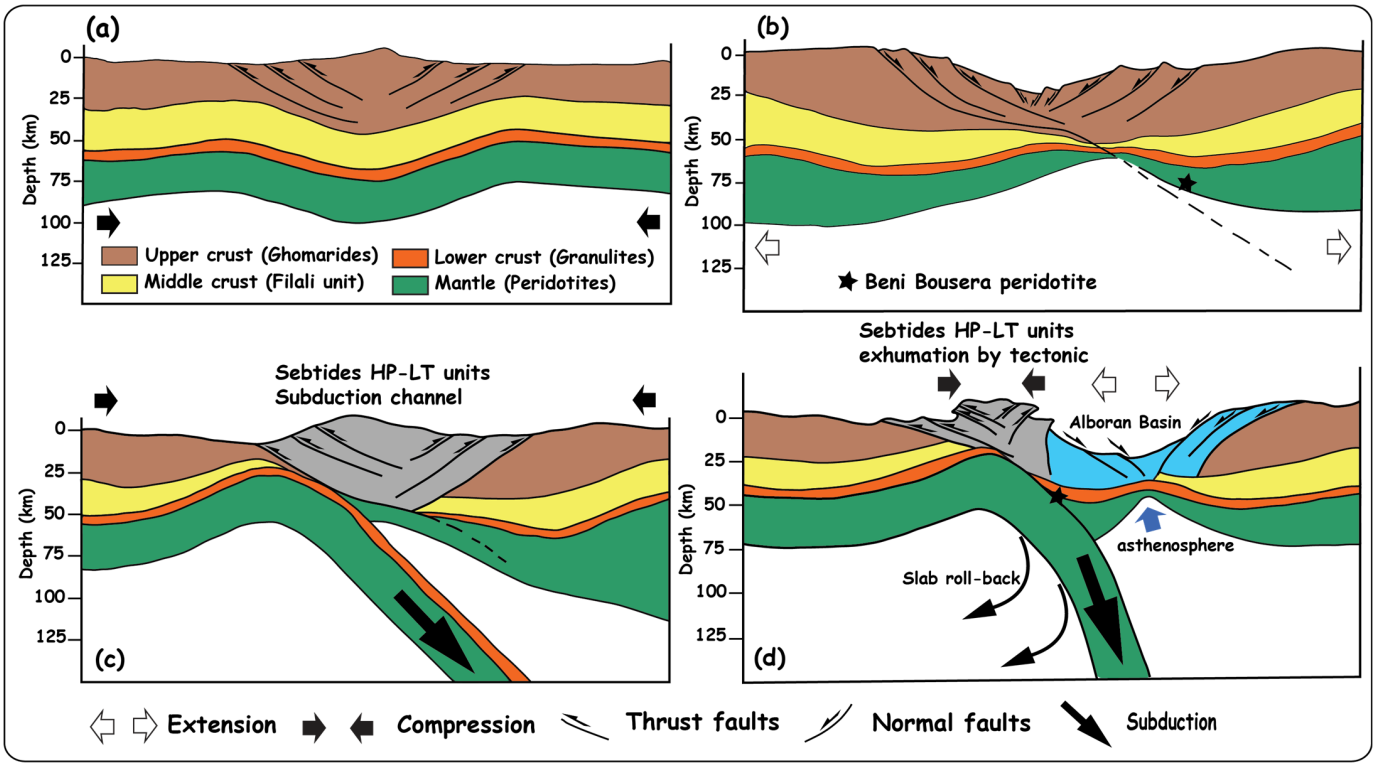

Figure 13. Synthetic geodynamic scenario for the emplacement of the Beni Bousera peridotite and the overlying crustal units of the Alboran domain, based on this study together with previous studies; (**a**) Permo-carboniferous: crustal thickening/shortening; (**b**) Early Jurassic: highly extended crust and upper mantle; (**c**) Upper Eocene–Oligocene; (**d**) Upper Oligocene–Early Miocene. See text for more details.

During the Early Eocene-Oligocene, the Alpine subduction led to the burial of Permo-Triassic sediments of this passive margin of the Upper Sebtides (Beni Mzela units) (Figure 13c) and some Alpujarrides units, as well as the Nevado–Filabride complex [90]. This subduction produced HP-LT metamorphism, where the peak pressure would be reached at around 25–30 Ma [11,33,90,91], whereas the Paleozoic basement consisted of the Ghomarides, Lower Sebtides, and Jubrique units. They only underwent HT-MP to LP metamorphism. The exhumation of the Upper Sebtides (HP/BT) occurred at 21.3 ± 1.7–20.9 ± 2.1 Ma (Beni Mzela units, monazite U-Th-Pb dating, and Ar/Ar and K/Ar micas ages) [11,73,90,92].

During the late Oligocene–early Miocene, lithospheric thinning occurred, led to the decompression phase of the Beni Bousera peridotite from mantle depths to the base of the crust (Figure 13d) [33], and induced HT-LP metamorphism. An extensional episode responsible for lithospheric thinning induced the partial melting of the lower crust and the emplacement of the granitic dykes (crossing the Lower Sebtides units) [21]. This episode would also have been responsible for the opening of the Alboran basin (Figure 13d) and the emplacement of sedimentary basins, e.g., [8]. The geodynamic scenario explaining the origin of the strong thinning remains unclear and may be related to the westward retreat of an Alpine subduction (slab roll-back) in a back-arc extensional context and upwelling of asthenospheric mantle [3,93–95], and/or a convective removal of the lithospheric mantle root [46,83,84,96]. Based on the P-T-t trajectories and the different tectonic reconstructions, we propose a model that brings the Beni Bousera peridotites to the surface late in the Lower Miocene by roll-back, as has been argued by other authors [3,51,93,97,98]. In such a geodynamic framework, subduction is initiated in the Upper Eocene–Oligocene, while in the Oligocene; the westward retreat of the subduction plane will cause the thinning of the upper plate, leading to the back-arc opening of the Alboran basin in the Western Mediterranean. Finally, brittle deformation materialized by normal faults, reflecting an

extensional context (Figure 13d), from the late Miocene era (Messinian) [99] to the present day led to the final opening of the Alboran Sea [33].

6. Conclusions

The results of this paper show that:

i. Three stages are recognized in the metamorphic evolution of the aluminous migmatitic paragneisses of the Filali unit, marked by the chemical zoning of garnet porphyroblasts and the evolution of associated mineral assemblages characterized by the presence of kyanite and rutile (M1), sillimanite, k-feldspar and melt (M2), and cordierite (M3). These mineralogical assemblages are characteristic of different geothermal gradients and, thus, different tectonic contexts.

ii. The main regional foliation S2 is consistent in the Filali metapelites (migmatitic gneiss, gneiss, and micaschists), granulite, and peridotite.

iii. In the migmatitic paragneisses, the syn-thermal peak assemblage associated with the main regional foliation S2 occurs under conditions of 7 kbar and 750 °C. These conditions are characteristic of MP-HT gradients. Geochronological data available on the Massif show that the age of the MP-HT metamorphic event (M2) is Oligo-Miocene. The M2 stage is coeval with the extensional D2 deformation responsible for an extreme lithospheric thinning of units previously thickened through collision.

iv. The P-T conditions of the early metamorphic peak assemblage (MP-MHT and foliation S1) are 9.3 kbar and 660 °C. These conditions were calculated by reintegrating the melt previously produced during the partial melting into the sillimanite stability field. They are established in the amphibolite facies and represent a metamorphic gradient of Barrovian type (20 °C/km). The pressure peak in the migmatitic paragneisses is related to crustal thickening associated with continental collision during the Variscan orogeny.

v. The P-T conditions of the retrograde assemblage are around 3.5 kbar and 685 °C. The cordierite-bearing retrograde assemblage is equilibrated in the amphibolite facies. The mineralogical assemblage of HT-MP is replaced by those of LP-HT in response to a sequence of strongly decompressive reactions, manifested along a sub-isothermal P-T path. This decompression is controlled by an extension in a back-arc context during the opening of the Alboran Sea. This is related to the westward retreat of an Alpine subduction (slab rollback), which is at the origin of the exhumation of the different units of the Lower and Upper Sebtides.

Author Contributions: Conceptualization, A.A. (Abdelkhaleq Afiri) and A.E.; methodology, A.A. (Abdelkhaleq Afiri); software, A.A. (Abdelkhaleq Afiri); validation, A.A. (Abdelkhaleq Afiri), A.C. and M.A. (Mourad Aqnouy); formal analysis, A.A. (Abdelkhaleq Afiri), K.A. and M.A. (Mohamed Abioui); investigation, A.A. (Abdelkhaleq Afiri); resources, A.A. (Abdelkhaleq Afiri); data curation, A.A. (Abdelkhaleq Afiri); writing—original draft preparation, A.A. (Abdelkhaleq Afiri); writing—review and editing, A.E., A.C., M.A. (Mourad Aqnouy), K.A., A.A. (Amar Alali) and M.A. (Mohamed Abioui); visualization, A.A. (Abdelkhaleq Afiri) and A.A. (Amar Alali); supervision, A.A. (Abdelkhaleq Afiri); project administration, M.A.(Mohamed Abioui); funding acquisition, K.A. All authors have read and agreed to the published version of the manuscript.

Funding: This research was funded by Researchers Supporting Project number (RSP2023R351), King Saud University, Riyadh, Saudi Arabia.

Data Availability Statement: Not applicable.

Conflicts of Interest: The authors declare no conflict of interest.

References

1. Do Couto, D.; Gorini, C.; Jolivet, L.; Jolivet, L.; Lebret, N.; Augier, R.; Gumiaux, C.; d'Acremont, E.; Ammar, A.; Jabour, H.; et al. Tectonic and stratigraphic evolution of the Western Alboran Sea Basin in the last 25 Myrs. *Tectonophysics* **2016**, *677–678*, 280–311. [CrossRef]
2. Lonergan, L.; White, N. Origin of the Betic-Rif mountain belt. *Tectonics* **1997**, *16*, 504–522. [CrossRef]

3. Faccenna, C.; Piromallo, C.; Crespo Blanc, A.; Jolivet, L.; Rosetti, F. Lateral slab deformation and the origin of the western Mediterranean arcs. *Tectonics* **2004**, *23*, TC1012. [CrossRef]
4. Jolivet, L.; Augier, R.; Faccenna, C.; Negro, F.; Rimmele, G.; Agard, P.; Robin, C.; Rossetti, F.; Crespo-Blanc, A. Subduction, convergence and the mode of back arc extension in the Mediterranean region. *Bull. Soc. Géol. Fr.* **2008**, *179*, 525–550. [CrossRef]
5. Vergés, J.; Fernàndez, M. Tethys–Atlantic interaction along the Iberia–Africa plate boundary: The Betic–Rif orogenic system. *Tectonophysics* **2012**, *579*, 144–172. [CrossRef]
6. Platt, J.P.; Behr, W.M.; Johanesen, K.; Williams, J.R. The Betic-Rif arc and its orogenic hinterland: A review. *Annu. Rev. Earth Planet. Sci.* **2013**, *41*, 313–357. [CrossRef]
7. Guerrera, F.; Martín-Martín, M.; Tramontana, M. Evolutionary geological models of the central-western peri-Mediterranean chains: A review. *Int. Geol. Rev.* **2019**, *63*, 65–86. [CrossRef]
8. Chalouan, A.; Michard, A.; El Kadiri, K.; Negro, F.; De Lamotte, D.F.; Soto, J.I.; Saddiqi, O. The Rif Belt. In *Continental Evolution: The Geology of Morocco: Structure, Stratigraphy, and Tectonics of the Africa-Atlantic-Mediterranean Triple Junction*; Michard, A., Saddiqi, O., Chalouan, A., Lamotte, D.F., Eds.; Springer: Berlin/Heidelberg, Germany, 2008; pp. 203–302. [CrossRef]
9. Gueydan, F.; Pitra, P.; Afiri, A.; Poujol, M.; Essaifi, A.; Paquette, J.L. Oligo-Miocene thinning of the Beni Bousera peridotites and their variscan crustal host rocks, Internal Rif, Morocco. *Tectonics* **2015**, *34*, 1244–1268. [CrossRef]
10. Michard, A.; Chalouan, A.; Feinberg, H.; Goffé, B.; Montigny, R. How does the Alpine belt end between Spain and Morocco? *Bull. Soc. Géol. Fr.* **2002**, *173*, 3–15. [CrossRef]
11. Michard, A.; Negro, F.; Saddiqi, O.; Bouybaouène, M.L.; Chalouan, A.; Montigny, R.; Goffé, B. Pressure-temperature-time constraints on the Maghrebide mountain building: Evidence from the Rif-Betic transect (Morocco, Spain), Algerian correlations, and geodynamic implications. *C. R. Geosci.* **2006**, *338*, 92–114. [CrossRef]
12. Montel, J.M.; Kornprobst, J.; Vielzeuf, D. Preservation of old U–Th–Pb ages in shielded monazite: Example from the Beni Bousera Hercynian kinzigites (Morocco). *J. Metamorph. Geol.* **2000**, *18*, 335–342. [CrossRef]
13. Rossetti, F.; Theye, T.; Lucci, F.; Bouybaouène, M.L.; Dini, A.; Gerdes, A.; Phillips, D.; Cozzupoli, D. Timing and modes of granite magmatism in the core of the Alboran Domain (rif chain, northern Morocco): Implications for the Alpine evolution of the western Mediterranea. *Tectonics* **2010**, *29*, TC2017. [CrossRef]
14. Rossetti, F.; Lucci, F.; Theye, T.; Bouybaouenne, M.L.; Gerdes, A.; Opitz, J.; Dini, A.; Lipp, C. Hercynian anatexis in the envelope of the Beni Bousera peridotites (Alboran Domain, Morocco): Implications for the tectono-metamorphic evolution of the deep crustal roots of the Mediterranean region. *Gondwana Res.* **2020**, *83*, 157–182. [CrossRef]
15. Massonne, H.J. Wealth of P–T–t information in medium-high grade metapelites: Example from the Jubrique Unit of the Betic Cordillera, S Spain. *Lithos* **2014**, *208–209*, 137–157. [CrossRef]
16. Melchiorre, M.; Álvarez-Valero, A.M.; Vergés, J.; Fernàndez, M.; Belousova, E.A.; El Maz, A.; Moukadiri, A. In situ U-Pb zircon geochronology on metapelitic granulites of Beni Bousera (Betic-Rif system, N Morocco). *Geol. Soc. Am. Spec. Pap.* **2017**, *526*, 151–171. [CrossRef]
17. Homonnay, E.; Corsini, M.; Lardeaux, J.-M.; Romagny, A.; Münch, P.; Bosch, D.; Cenki-Tok, B.; Ouazzani-Touhami, M. Miocene crustal extension following thrust tectonic in the Lower Sebtides units (internal Rif, Ceuta Peninsula, Spain): Implication for the geodynamic evolution of the Alboran domain. *Tectonophysics* **2018**, *722*, 507–535. [CrossRef]
18. El Bakili, A. Evolution Tectono-métamorphique et Chronologique des Unités Métamorphiques du Rif Interne (Béni Bousera, Nord du Maroc). Ph.D. Thesis, Université Côte d'Azur, Nice, France, 2021.
19. Obata, M. The Ronda peridotite: Garnet-, spinel-, and plagioclase-lherzolite facies and the P-T trajectories of a high-temperature mantle intrusion. *J. Petrol.* **1980**, *21*, 533–572. [CrossRef]
20. Van der Wal, D.; Vissers, R.L.M. Uplift and emplacement of upper mantle rocks in the western Mediterranean. *Geology* **1993**, *21*, 1119–1122. [CrossRef]
21. Rossetti, F.; Dini, A.; Lucci, F.; Bouybaouène, M.L.; Faccenna, C. Early Miocene strike slip tectonics and granite emplacement in the Alboran Domain (Rif Chain, Morocco): Significance for the geodynamic evolution of Western Mediterranean. *Tectonophysics* **2013**, *608*, 774–791. [CrossRef]
22. Casciello, E.; Fernández, M.; Vergés, J.; Cesarano, M.; Torné, M. The Alboran Domain in the Western Mediterranean evolution: The birth of a concept. *Bull. Soc. Géol. Fr.* **2015**, *186*, 23–34. [CrossRef]
23. White, R.W.; Powell, R.; Holland, T.J.B. Progress relating to calculation of partial melting equilibria for metapelites. *J. Metamorph. Geol.* **2007**, *25*, 511–527. [CrossRef]
24. Powell, R.; Guiraud, M.; White, R.W. Truth and beauty in metamorphic phase equilibria: Conjugate variables and phase diagrams. *Can. Mineral.* **2005**, *43*, 21–33. [CrossRef]
25. White, R.W.; Powell, R. Melt loss and the preservation of granulite facies mineral assemblages. *J. Metamorph. Geol.* **2002**, *20*, 621–632. [CrossRef]
26. White, R.W.; Powell, R.; Halpin, A. Spatially-focused melt formation in aluminous metapelites from Broken Hill, Australia. *J. Metamorph. Geol.* **2004**, *22*, 825–845. [CrossRef]
27. Indares, A.D.; White, R.W.; Powell, R. Phase equilibria modelling of kyanite-bearing anatectic paragneisses from the central Grenville Province. *J. Metamorph. Geol.* **2008**, *26*, 815–836. [CrossRef]
28. Guilmette, C.; Indares, A.; Hebert, R. High-pressure anatectic paragneisses from the Namche Barwa, Eastern Himalayan Syntaxis: Textural evidence for partial melting, phase equilibria modelling and tectonic implications. *Lithos* **2011**, *124*, 66–81. [CrossRef]

29. Balanyá, J.C.; García-Dueñas, V. Les directions structurales dans le Domaine d'Alboran de part et d'autre du Détroit de Gibraltar. *C. R. Acad.Sci.* **1987**, *304*, 929–933.
30. Augier, R.; Agard, P.; Monié, P.; Jolivet, L.; Robin, C.; Booth-Rea, G. Exhumation, doming and slab retreat in the Betic Cordillera (SE Spain): In situ 40Ar/39Ar ages and P–T–d–t paths for the Nevado-Filabride complex. *J. Metamorph. Geol.* **2005**, *23*, 357–381. [CrossRef]
31. Negro, F.; Beyssac, O.; Goffé, B.; Saddiqi, O.; Bouybaouène, M.L. Thermal structure of the Alboran Domain in the Rif (northern Morocco) and the Western Betics (southern Spain). Constraints from Raman spectroscopy of carbonaceous material. *J. Metamorph. Geol.* **2006**, *24*, 309–327. [CrossRef]
32. El Maz, A.; Guiraud, M. Paragenèse à faible variance dans les mètapèlites de la série de Filali (Rif interne marocain): Description, interprétation et conséquences géodynamiques. *Bull. Soc. Géol. Fr.* **2001**, *172*, 469–485. [CrossRef]
33. Afiri, A.; Gueydan, F.; Pitra, P.; Essaifi, A.; Précigout, J. Oligo-Miocene exhumation of the Beni-Bousera peridotite through a lithosphere-scale extensional shear zone. *Geodin. Acta* **2011**, *24*, 49–60. [CrossRef]
34. Bouybaouène, M.L.; Goffé, B.; Michard, A. High pressure, low-temperature metamorphism in the Sebtides nappes, northern Rif, Morocco. *Geogaceta* **1995**, *17*, 117–119.
35. Goffé, B.; Azañon, J.M.; Bouybaouène, M.L.; Jullien, M. Metamorphic cookeite in Alpine metapelites from Rif, northern Morocco, and the Betic Chain, southern Spain. *Eur. J. Mineral.* **1996**, *8*, 335–348. [CrossRef]
36. Bouybaouène, M.L.; Goffé, B.; Michard, A. High-pressure granulites on top of the Beni Bousera peridotites, Rif belt, Morocco: A record of an ancient thickened crust in the Alboran domain. *Bull. Soc. Géol. Fr.* **1998**, *169*, 153–162.
37. Haissen, F.; Garcia-Casco, A.; Torres-Roldan, R.; Aghzer, A. Decompression reactions and P-T conditions in high-pressure granulites from Casares-Los Reales units of the Betic-Rif belt (S Spain and N Morocco). *J. Afr. Earth Sci.* **2004**, *39*, 375–383. [CrossRef]
38. Álvarez-Valero, A.M.; Jagoutz, O.; Stanley, J.; Manthei, C.; El Maz, A.; Moukadiri, A.; Piasecki, A. Crustal attenuation as a tracer for the emplacement of the Beni Bousera ultramafic massif (Betico-Rifean belt). *Geol. Soc. Am. Bull.* **2014**, *126*, 1614–1624. [CrossRef]
39. Kornprobst, J. Contribution à l'étude pétrographique et structurale de la zone interne du Rif (Maroc septentrional)[Petrography and structure of the Rif inner area, northern Morocco]. *Notes Mèm. Serv. Géol. Maroc* **1974**, *251*, 256p.
40. Reuber, I.; Michard, A.; Chalouan, A.; Juteau, T.; Jermoumi, B. Structure and emplacement of the Alpine-type peridotites from Beni Bousera, Rif, Morocco: A polyphase tectonic interpretation. *Tectonophysics* **1982**, *82*, 231–251. [CrossRef]
41. Saddiqi, O.; Reuber, I.; Michard, A. Sur la tectonique de dénudation du manteau infracontinental dans les Béni Bousera, Rif septentrional, Maroc. *C. R. Acad. Sci.* **1988**, *307*, 657–662.
42. Tornè, M.; Banda, E.; Garcia-Duenas, V.; Balanyá, J.C. Mantle-lithosphere bodies in the Alboran crustal domain (Ronda peridotites, Betic-Rif orogenic belt). *Earth Planet. Sci. Lett.* **1992**, *110*, 163–171. [CrossRef]
43. Pearson, D.G.; Davies, G.R.; Nixon, P.H.; Milledge, H.J. Graphitized diamonds from a peridotite massif in Morocco and implications for anomalous diamond occurrences. *Nature* **1989**, *335*, 60–66. [CrossRef]
44. Davies, G.R.; Nixon, P.H.; Pearson, D.G.; Obata, M. Tectonic implications of graphitized diamonds from the Ronda peridotite massif, southern Spain. *Geology* **1993**, *21*, 471–474. [CrossRef]
45. El Atrassi, F.; Brunet, F.; Bouybaouène, M.L.; Chopin, C.; Chazot, G. Melting textures and microdiamonds preserved in graphite pseudomorphs from the Beni Bousera peridotite massif, Morocco. *Eur. J. Mineral.* **2011**, *23*, 157–168. [CrossRef]
46. Platt, J.P.; Vissers, R.M.S. Extensional collapse of the thickened continental lithosphere: A working hypothesis for the Alboran Sea and Gibraltar arc. *Geology* **1989**, *17*, 540–543. [CrossRef]
47. Seber, D.; Barazangi, M.; Ibenbrahim, A.; Demnati, A. Geophysical evidence for lithospheric delamination beneath the Alboran Sea and Rif-Betic mountains. *Nature* **1996**, *379*, 785–790. [CrossRef]
48. Calvert, A.; Sandvol, E.; Seber, D.; Barazangi, M.; Roecker, S.; Mourabit, T.; Vidal, F.; Alguacil, G.; Jabour, N. Geodynamic evolution of the lithosphere and upper mantle beneath the Alboran region of the western Mediterranean: Constraints from travel time tomography. *J. Geophys. Res.* **2000**, *105*, 10871–10898. [CrossRef]
49. Balanyá, J.C.; Azañon, J.M.; Sánchez-Gomez, M.; Garcia-Dueñas, V. Pervasive ductile extension, isothermal decompression and thinning of the Jubrique Unit in the Paleogene (Alpujarride Complex, western Betics, Spain). *C. R. Acad. Sci.* **1993**, *316*, 1595–1601.
50. Sánchez-Rodriguez, L.; Gebauer, D. Mesozoic formation of pyroxenites and gabbros in the Ronda area (southern Spain), followed by early Miocene subduction metamorphism and emplacement into the middle crust: U-Pb sensitive high-resolution ion microprobe dating of zircon. *Tectonophysics* **2000**, *316*, 19–44. [CrossRef]
51. Van Hinsbergen, D.J.J.; Vissers, R.L.M.; Spakman, W. Origin and consequences of western Mediterranean subduction, rollback, and slab segmentation. *Tectonics* **2014**, *33*, 393–419. [CrossRef]
52. Hidas, K.; Booth-Rea, G.; Garrido, C.J.; Martínez-Martínez, J.M.; Padrón-Navarta, J.A.; Konc, Z.; Giaconia, F.; Frets, E.; Marchesi, C. Back arc basin inversion and subcontinental mantle emplacement in the crust: Kilometre-scale folding and shearing at the base of the proto-Alborán lithospheric mantle (Betic Cordillera, southern Spain). *J. Geol. Soc.* **2013**, *170*, 47–55. [CrossRef]
53. Azdimousa, A.; Bourgois, J.; Poupeau, G.; Vázquez, M.; Asebriy, L.; Labrin, E. Fission track thermochronology of the Beni Bousera peridotite massif (Internal Rif, Morocco) and the exhumation of ultramafic rocks in the Gibraltar Arc. *Arab. J. Geosci.* **2014**, *7*, 1993–2005. [CrossRef]

54. El Bakili, A.; Corsini, M.; Chalouan, A.; Münch, P.; Romagny, A.; Lardeaux, J.M.; Azdimousa, A. Neogene polyphase deformation related to the Alboran basin evolution: New insights for the Beni Bousera massif (Internal Rif, Morocco). *BSGF-Earth Sci. Bull.* **2020**, *191*, 10. [CrossRef]
55. Afiri, A. Étude Pétro-Structurale des Péridotites de Béni Bousera et des Roches Crustales Sus-Jacentes (Rif Interne, Maroc): Implications Géodynamiques. Ph.D. Thesis, Université Cadi Ayyad, Marrakech, Morocco, 2011.
56. Sawyer, E.W. *Atlas of Migmatites*; The Canadian Mineralogist Special Publication (Volume 9); NRC Research Press: Ottawa, ON, Canada, 2008; 371p.
57. Spear, F.S. Metamorphic fractional crystallization and internal metasomatism by diffusional homogenization of zoned garnets. *Contrib. Mineral. Petrol.* **1988**, *99*, 507–517. [CrossRef]
58. Holland, T.J.B.; Powell, R. An internally consistent thermodynamic data set for phases of petrological interest. *J. Metamorph. Geol.* **1998**, *16*, 309–343. [CrossRef]
59. Powell, R.; Holland, T.J.B. An internally consistent dataset with uncertainties and correlations: 3. Applications to geobarometry, worked examples and a computer program. *J. Metamorph. Geol.* **1988**, *6*, 173–204. [CrossRef]
60. Holland, T.J.B.; Powell, R. *AX: A Program to Calculate Mineral End-Members from Chemical Analyses (Usually from an Electron Microprobe)*; Cambridge University Press: Cambridge, UK, 2000.
61. Powell, R.; Holland, T.J.B. *Course Notes for "THERMOCALC Workshop 2002: Calculating Metamorphic Phase Equilibria"* [CD-ROM]; 2002.
62. Coggon, R.; Holland, T.J.B. Mixing properties of phengitic micas and revised garnet-phengite thermobarometers. *J. Metamorph. Geol.* **2002**, *20*, 683–696. [CrossRef]
63. Holland, T.J.B.; Powell, R. Activity-composition relations for phases in petrological calculations: An asymmetric multicomponent formulation. *Contrib. Mineral. Petrol.* **2003**, *145*, 492–501. [CrossRef]
64. White, R.W.; Powell, R.; Holland, T.J.B.; Worley, B.A. The effect of TiO_2 and Fe_2O_3 on metapelitic assemblages at green schist and amphibolite facies conditions: Mineral equilibria calculations in the system K_2O-FeO-MgO-Al_2O_3-SiO_2-H_2O-TiO_2-Fe_2O_3. *J. Metamorph. Geol.* **2000**, *18*, 497–511. [CrossRef]
65. Korhonen, F.J.; Brown, M.; Clark, C.; Bhattacharya, S. Osmulite–melt interactions in ultrahigh temperature granulites: Phase equilibria modelling and implications for the P–T–t evolution of the Eastern Ghats Province, India. *J. Metamorph. Geol.* **2013**, *31*, 881–907. [CrossRef]
66. Yakymchuk, C.; Brown, M. Consequences of open system melting in tectonics. *J. Geol. Soc.* **2014**, *171*, 21–40. [CrossRef]
67. Rosenberg, C.L.; Handy, M.R. Experimental deformation of partially melted granite revisited: Implications for the continental crust. *J. Metamorph. Geol.* **2005**, *23*, 19–28. [CrossRef]
68. Fernández, R.D.; Arenas, R.; Pereira, M.F.; Sánchez-Martínez, S.; Albert, R.; Parra, L.M.M.; Rubio Pascual, F.J.; Matas, J. Tectonic evolution of Variscan Iberia: Gondwana–Laurussia collision revisited. *Earth-Sci. Rev.* **2016**, *162*, 269–292. [CrossRef]
69. Sánchez-Rodríguez, L. Alpine Evolution of the Ronda Ultramafic Complex and Its Country-Rocks (Betic Chain, Southern Spain): U-Pb SHRIMP Zircon and Fission-Track Dating. Ph.D. Thesis, Swiss Federal Institute of Technology, Zürich, Switzerland, 1998.
70. Ruiz Cruz, M.D.; Sanz de Galdeano, C. Garnet variety and zircon ages in UHP meta-sedimentary rocks from the Jubrique zone (Alpujárride Complex, Betic Cordillera, Spain): Evidence for a pre-Alpine emplacement of the Ronda peridotite. *Int. Geol. Rev.* **2014**, *56*, 845–868. [CrossRef]
71. Michard, A.; Goffé, B.; Bouybaouène, M.L.; Saddiqi, O. Late Hercynian Mesozoic thinning in the Alboran domain: Metamorphic data from the northern Rif, Morocco. *Terra Nova* **1997**, *9*, 171–174. [CrossRef]
72. Zeck, H.P.; Whitehouse, M.J. Repeated age resetting in zircons from Hercynian–Alpine polymetamorphic schists (Betic–Rif tectonic belt, S. Spain)-a U–Th–Pb ion microprobe study. *Chem. Geol.* **2002**, *182*, 275–292. [CrossRef]
73. Whitehouse, M.J.; Platt, J.P. Dating high-grade metamorphism—Constraints from rare-earth elements in zircon and garnet. *Contrib. Mineral. Petrol.* **2003**, *145*, 61–74. [CrossRef]
74. Michard, A.; Chalouan, A.; Montigny, R.; Ouazzani-Touhami, M. Les nappes cristallophylliennes du Rif (Sebtides, Maroc), témoins d'un édifice alpin de type pennique incluant le manteau supérieur. *C. R. Acad. Sci.* **1983**, *296*, 1337–1340.
75. Michard, A.; Goffé, B.; Chalouan, A.; Saddiqi, O. Les corrélations entre les chaînes Bètico-Rifaines et les Alpes et leurs conséquences. *Bull. Soc. Géol. Fr.* **1991**, *162*, 1151–1160.
76. Comas, M.C.; Platt, J.P.; Soto, J.I.; Watts, A.B. The origin and tectonic history of the Alboran Basin: Insights from Leg 161 results. In *Proceedings of the Ocean Drilling Program Scientific Results*; Zahn, R., Comas, M.C., Klaus, A., Eds.; Ocean Drilling Program: College Station, TX, USA, 1999; Volume 161, pp. 555–580.
77. Acosta-Vigil, A.; Rubatto, D.; Bartoli, O.; Cesare, B.; Meli, S.; Pedrera, A.; Azor, A.; Tajčmanová, L. Age of anatexis in the crustal footwall of the Ronda peridotites, S Spain. *Lithos* **2014**, *210–211*, 147–167. [CrossRef]
78. Sánchez-Navas, A.; García-Casco, A.; Mazzoli, S.; Martín-Algarra, A. Polymetamorphism in the Alpujarride Complex, Betic Cordillera, South Spain. *J. Geol.* **2017**, *125*, 637–657. [CrossRef]
79. Kornprobst, J. Signification structurale des péridotites dans l'orogenèse bético-rifain: Arguments tirés de l'étude des détritus observés dans les sédiments paléozoïques. *Bull. Soc. Géol. Fr.* **1976**, *7*, 607–618. [CrossRef]
80. Sanz de Galdeano, C.; Ruiz-Cruz, M.D. Late Palaeozoic to Triassic formations unconformably deposited over the Ronda peridotites (Betic Cordilleras): Evidence for their Variscan time of crustal emplacement. *Estud. Geol.* **2016**, *72*, e043. [CrossRef]

81. Farah, A.; Michard, A.; Saddiqi, O.; Chalouan, A.; Chopin, C.; Montero, P.; Corsini, M.; Bea, F. The Beni Bousera marbles, record of a Triassic-Early Jurassic hyperextended margin in the Alpujarrides-Sebtides units (Rif belt, Morocco). *BSGF-Earth Sci. Bull.* **2021**, *192*, 26. [CrossRef]
82. Tubía, J.M.; Cuevas, J.; Esteban, J.J. Localization of deformation and kinematic shift during the hot emplacement of the Ronda Peridotites (Betic Cordilleras, southern Spain). *J. Struct. Geol.* **2013**, *50*, 148–160. [CrossRef]
83. Platt, J.P.; Whitehouse, M.J.; Kelley, S.P.; Carter, A.; Hollick, L. Simultaneous extensional exhumation across the Alboran Basin: Implications for the causes of late orogenic extension. *Geology* **2003**, *31*, 251–254. [CrossRef]
84. Platt, J.P.; Argles, T.W.; Carter, A.; Kelley, S.P.; Whitehouse, M.J.; Lonergan, L. Exhumation of the Ronda peridotite and its crustal envelope: Constraints from thermal modelling of a P–T–time array. *J. Geol. Soc.* **2003**, *160*, 655–676. [CrossRef]
85. Garrido, C.J.; Gueydan, F.; Booth-Rea, G.; Precigout, J.; Hidas, K.; Padrón-Navarta, J.A.; Marchesi, C. Garnet lherzolite and garnet-spinel mylonite in the Ronda peridotite: Vestiges of Oligocene backarc mantle lithospheric extension in the western Mediterranean. *Geology* **2011**, *39*, 927–930. [CrossRef]
86. Mazzoli, S.; Martín-Algarra, A. Deformation partitioning during transpressional emplacement of a 'mantle extrusion wedge': The Ronda Peridotites, Western Betic Cordillera, Spain. *J. Geol. Soc. Lond.* **2011**, *168*, 373–382. [CrossRef]
87. Gueydan, F.; Mazzotti, S.; Tiberi, C.; Cavin, R.; Villaseñor, A. Western Mediterranean subcontinental mantle emplacement by continental margin obduction. *Tectonics* **2019**, *38*, 2142–2157. [CrossRef]
88. Chalouan, A.; Michard, A. The Alpine Rif belt (Morocco): A case of mountain building in a subduction-subduction-transform fault triple junction. *Pure Appl. Geophys.* **2004**, *161*, 489–519. [CrossRef]
89. Pearson, D.G.; Davies, G.R.; Nixon, P.H. Geochemical constraints on the petrogenesis of diamond facies pyroxenites from the Beni Bousera peridotite massif, north Morocco. *J. Petrol.* **1993**, *34*, 125–172. [CrossRef]
90. Marrone, S.; Monié, P.; Rossetti, F.; Lucci, F.; Theye, T.; Bouybaouène, M.L.; Zaghloul, M.N. The pressure-temperature-time-deformation history of the Beni Mzala unit (Upper Sebtides, Rif belt, Morocco): Refining the Alpine tectono-metamorphic evolution of the Alboran Domain of the western Mediterranean. *J. Metamorph. Geol.* **2021**, *39*, 591–615. [CrossRef]
91. Azañon, J.M.; Goffé, B. Ferro-and magnesio carpholite assemblages as record of high-P, low-T metamorphism in the central Alpujarrides, Betic Cordillera (SE Spain). *Eur. J. Mineral.* **1997**, *9*, 1035–1051. [CrossRef]
92. Janots, E.; Negro, F.; Brunet, F.; Goffé, B.; Engi, M.; Bouybaouène, M.L. Evolution of the REE mineralogy in HP-LT metapelites of the Sebtides complex, Rif, Morocco: Monazite stability and geochronology. *Lithos* **2006**, *87*, 214–234. [CrossRef]
93. Jolivet, L.; Faccenna, C. Mediterranean extension and the Africa-Eurasia collision. *Tectonics* **2000**, *19*, 1095–1106. [CrossRef]
94. Duggen, S.; Hoernle, K.; van den Bogaard, P.; Harris, C. Magmatic evolution of the Alboran region: The role of subduction in forming the western Mediterranean and causing the Messinian Salinity Crisis. *Earth Planet. Sci. Lett.* **2004**, *218*, 91–108. [CrossRef]
95. Lacombe, O.; Jolivet, L. Structural and kinematic relationships between Corsica and the Pyrenees-Provence domain at the time of the Pyrenean orogeny. *Tectonics* **2005**, *24*, TC1003. [CrossRef]
96. Platt, J.P.; Kelley, S.P.; Carter, A.; Orozco, M. Timing of tectonic events in the Alpujárride Complex, Betic Cordillera, southern Spain. *J. Geol. Soc.* **2005**, *162*, 451–462. [CrossRef]
97. Spakman, W.; Wortel, R. Tomographic view on western Mediterranean geodynamics. In *The TRANSMED Atlas, The Mediterranean Region from Crust to Mantle*; Cavazza, W., Ed.; Springer: Berlin/Heidelberg, Germany, 2004; pp. 31–52. [CrossRef]
98. Bezada, M.J.; Humphreys, E.D.; Toomey, D.R.; Harnafi, M.; Dávila, J.M.; Gallart, J. Evidence for slab rollback in westernmost Mediterranean from improved upper mantle imaging. *Earth Planet. Sci. Lett.* **2013**, *368*, 51–60. [CrossRef]
99. Romagny, A. Évolution des Mouvements Verticaux Néogènes de la Chaîne du Rif (Nord Maroc): Apports d'une Analyse Structurale et Thermochronologique. Ph.D. Thesis, Université de Nice Sophia-Antipolis, Nice, France, 2014.